nature physics

Article

https://doi.org/10.1038/s41567-026-03277-5

Superconductivity from dual-surface carriers in rhombohedral graphene

Received: 26 October 2025

Accepted: 30 March 2026

Published online: 5 June 2026

Check for updates

Manish Kumar[1,9], Derek Waleffe[1,9], Anna Okounkova[1,9], Raveel Tejani[2,3], Võ Tiến Phong[4,5], Kenji Watanabe[6], Takashi Taniguchi[7], Cyprian Lewandowski[4,5], Joshua Folk[2,3] ✉ & Matthew Yankowitz[1,8] ✉

Rhombohedral graphene at charge neutrality hosts an unusual low-energy electronic wavefunction that is predominantly localized at its top and bottom layers and has negligible presence in the bulk. Increasing the number of graphene layers amplifies the density of states near charge neutrality and thereby enhances the susceptibility to symmetry-breaking phases. Here we report superconductivity in rhombohedral graphene arising from this charge-delocalized semimetallic normal state, which is characterized by coexisting valence- and conduction-band Fermi pockets split over opposite crystal surfaces. In octalayer graphene, the superconductivity appears in five apparently distinct regions of the phase diagram for each sign of an external electric displacement field. In a moiré superlattice sample where heptalayer graphene is aligned on one side to hexagonal boron nitride, two regions of superconductivity emerge from a single sharp resistive feature. At higher displacement field, the same resistive feature additionally induces an anomalous Hall state quantized at h/e^2 when the doping is close to one electron per moiré unit cell. Our findings highlight the various superconducting regimes in multilayer graphene and create opportunities for coupling to nearby topological states.

Chiral stacking of graphene in the metastable rhombohedral (ABC) configuration gives rise to unique low-energy electronic properties characterized by flat bands and non-trivial topology[1–5]. Much of the existing work on this material has focused on new ground states that emerge when a sizeable interlayer displacement field (D) opens a gap at the charge neutrality point (CNP)[6]. Within this gapped regime, the enhanced density of states (DOS) near the valence- and conduction-band edges promotes superconductivity[7–17] along with spontaneous spin or valley polarization in line with the Stoner criterion[8,18–21]. Recently, compelling signatures of chiral superconductivity have been observed at small electron doping of the flat conduction-band edge in four- to six-layer samples[15,17]. When a superlattice potential is further introduced by close rotational alignment of graphene with hexagonal boron nitride (hBN), many-body gaps open at commensurate filling factors of the moiré unit cell. Over a similar range of doping and displacement field that hosts the putative chiral superconductivity in misaligned samples, moiré devices instead exhibit integer quantum anomalous Hall (IQAH) and fractional quantum anomalous Hall states[22–26].

The regime of small interlayer potentials, in which the valence and conduction bands overlap at the Fermi level to form a semimetal, also hosts a large DOS yet remains far less explored. Substantial

[1]Department of Physics, University of Washington, Seattle, WA, USA. [2]Department of Physics and Astronomy, University of British Columbia, Vancouver, British Columbia, Canada. [3]Quantum Matter Institute, University of British Columbia, Vancouver, British Columbia, Canada. [4]National High Magnetic Field Laboratory, Tallahassee, FL, USA. [5]Department of Physics, Florida State University, Tallahassee, FL, USA. [6]Research Center for Electronic and Optical Materials, National Institute for Materials Science, Tsukuba, Japan. [7]Research Center for Materials Nanoarchitectonics, National Institute for Materials Science, Tsukuba, Japan. [8]Department of Materials Science and Engineering, University of Washington, Seattle, WA, USA. [9]These authors contributed equally: Manish Kumar, Derek Waleffe, Anna Okounkova. ✉e-mail: jfolk@physics.ubc.ca; myank@uw.edu

https://doi.org/10.1038/s41567-026-03277-5

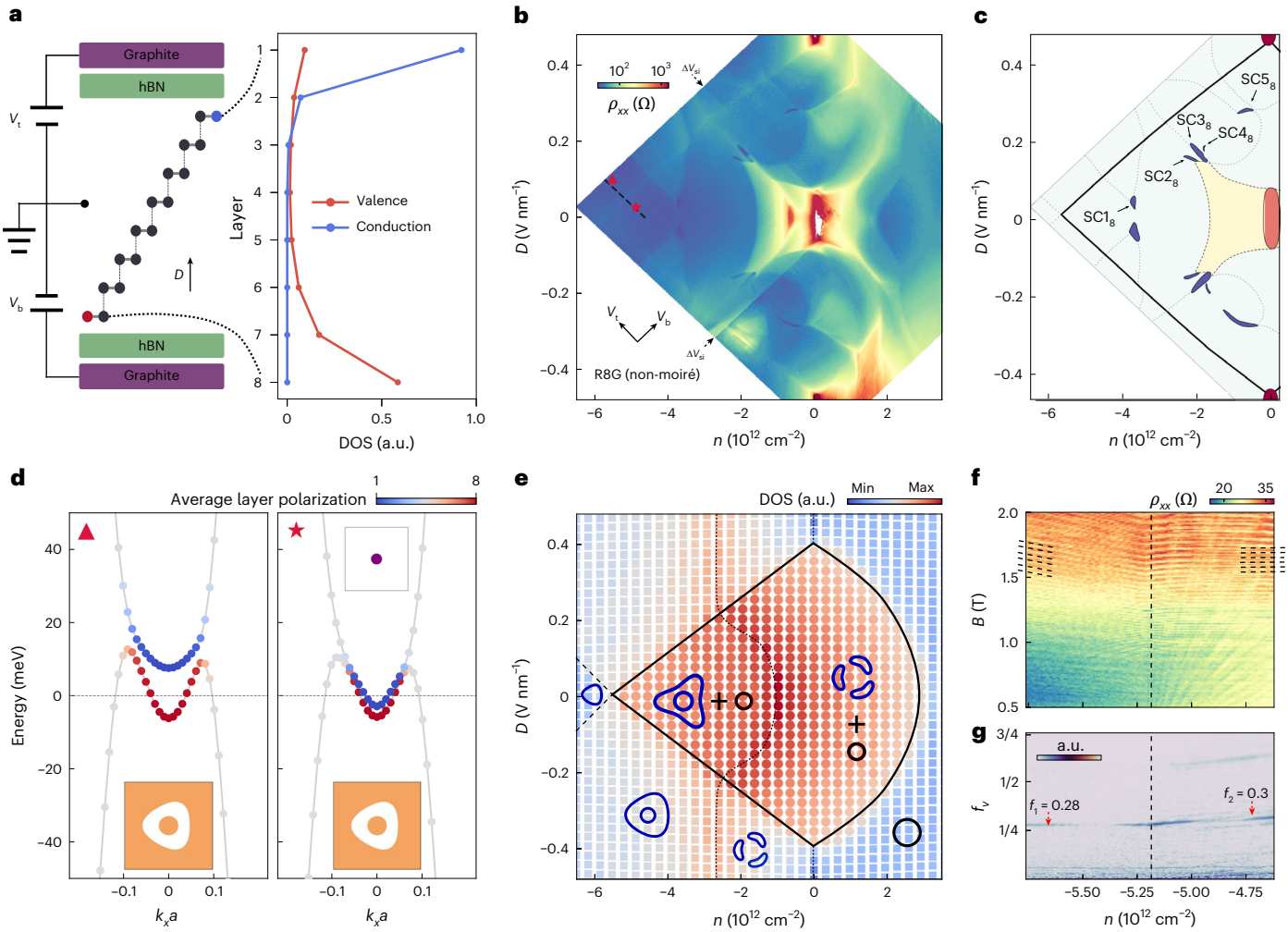

Fig. 1 | Semimetallic properties of rhombohedral graphene and transport in an R8G device. a, Left: schematic of a unit cell of R8G. Red and blue denote the atoms that do not form dimers. The R8G is encapsulated by hBN on both sides, with graphite top and bottom gates. Right: calculated DOS resolved by layer number for the valence and conduction bands at $n = -1.95 \times 10^{12}$ cm^{-2} and $D = 0.178$ V nm^{-1}. **b**, Measurement of ρ_{xx} versus n and D in an R8G sample without hBN alignment. Arrows denote measurement artefacts (along fixed V_t and V_b) arising from the change in silicon gate bias, ΔV_{si}. **c**, Schematic denoting some of the key transport features seen in **b**. Band insulators (correlated insulator) at the CNP are denoted in red (dark orange). The light orange indicates a symmetry-broken metallic phase adjacent to the CNP. Dashed and solid lines trace the positions of resistive bump features. Blue pockets correspond to superconductivity. **d**, Calculated band structure (k_x is the wavenumber and $a = 2.46$ Å is the graphene lattice constant), at $n = -5.52 \times 10^{12}$ cm^{-2} and $D = 0.1$ V nm^{-1} (left) and $n = -4.87 \times 10^{12}$ cm^{-2} and $D = 0.026$ V nm^{-1} (right), corresponding to the red triangle and square in **b**, respectively. The colour coding indicates the average layer polarization of each state. The top (bottom) inset shows the constant energy contour of the conduction (valence) band at the Fermi energy ($E = 0$). White colouring indicates empty states. **e**, Map of the calculated DOS at E_F. Solid and dashed lines trace out local maxima or abrupt steps in the DOS, and they separate regions of parameter space with distinct Fermi-surface topologies (shown in blue and black for the valence and conduction bands, respectively). The solid black curve traces the crossover between the band-overlapping region (circular data points) and band-isolated region (square data points), and can be compared directly with the black lines in **c**. **f**, Landau fan diagram measured by sweeping V_t for fixed $V_b = -6.0$ V, corresponding to the black dashed line in **b**. **g**, Fourier transform of the data in **f**, plotted as a function of f_ν (frequency normalized by the Luttinger volume, $n(h/e)$). f_1 and f_2 denote the dominant frequency in the band-isolated and band-overlapping regimes, respectively. min, minimum; max, maximum.

charge doping and displacement field are required to move the Fermi energy E_F out of this semimetallic regime, creating a sizeable area of parameter space in which rhombohedral multilayer graphene acts as a strongly correlated semimetal. Figure 1a shows a schematic of a rhombohedral octalayer graphene (R8G) device next to a calculation of the layer-resolved DOS at a doping of $n = -1.95 \times 10^{12}$ cm^{-2} and $D = 0.178$ V nm^{-1}. The conduction band is exponentially localized on the top layer. The valence band is predominantly localized on the bottom layer, but decays more slowly into the bulk before showing a small secondary peak on the top layer. This behaviour can be understood in analogy with the topological edge states of the Su–Schrieffer–Heeger chain model[1,2,6,27], and it demonstrates the propensity for charges in rhombohedral graphene to occupy both surfaces simultaneously with minimal density in the central layers. The bifurcated charge distribution is distinct from that of conventional semimetals, in which electron- and hole-like carriers exhibit a substantial spatial overlap.

Our main observation is that this distinctive semimetallic normal state hosts pockets of superconductivity for which the distribution of the wavefunction along the c axis emerges as a crucial degree of freedom that affects the pairing. In the moiré superlattice sample, the superconductivity emerges from a feature associated with the conduction band in the semimetallic region at small D, which then evolves to an IQAH state at large D with transverse resistance quantized to $\pm h/e^2$, where h is the Planck constant and e the elementary charge.

Dual-surface charge distribution

We first established the phase boundaries separating the semimetallic region of rhombohedral graphene from regions where the Fermi level crosses only one band. We did this by comparing transport measurements with band-structure and Hartree–Fock calculations (full details provided in Methods and Supplementary Information Section II). Although we focused on R8G, our discussion generalizes to a broad range of layer numbers.

Figure 1b shows the longitudinal resistivity (ρ_{xx}) measured for an R8G sample acquired by independently varying the top- and bottom-gate voltages, V_t and V_b, and converting the values to n and D through a standard linear mapping (Methods and Extended Data Fig. 1). The data reproduce several features familiar from earlier studies of rhombohedral graphene, including band insulators at the CNP at large D, a correlated insulator at the CNP centred around $D = 0$ (refs. 19,20,28–30) and a surrounding region of elevated resistance that has been associated with a symmetry-broken phase[31]. Figure 1c is a schematic diagram of these and other key features.

Separately, we calculated the band structure (for example, Fig. 1d) to visualize the layer polarization of the bands and to generate a map of the DOS at the Fermi energy (Fig. 1e). Crucially, each point in this map was obtained from a self-consistent electrostatic calculation, which enabled an accurate conversion to the experimentally relevant n and D values[32] (Methods). The calculation predicted a contiguous region surrounding the CNP and centred about $D = 0$ in which the Fermi level crosses through both the valence and conduction bands. The boundaries of this region are denoted by the solid black outline superimposed on the map in Fig. 1e. Inside this region, Fermi surfaces for the valence band (blue) coexist with those for the conduction band (black). Outside, representative sketches illustrate the changing topology of the single Fermi surfaces with n and D.

The calculation reproduces several salient features of the experiment. Notably, the transport map exhibits diagonal jets of weakly enhanced ρ_{xx} that emerge upon opening the large-D gap at charge neutrality. These jets follow trajectories of nearly fixed V_t or V_b for $n < 0$, denoted by the solid black lines in Fig. 1c, that closely correspond to the equivalent segments of the outline in the DOS map. Thus, we interpret these jets as enclosing the region of n–D space in which the R8G is a semimetal.

To support this interpretation, we examine a Landau fan diagram taken along the black dashed line in Fig. 1b, which crosses one of the jets. The magnetic field (B) and V_t were swept at fixed V_b (Fig. 1f). The quantum oscillations (QOs) at very negative n follow the Středa formula, which projects to $n = 0$ at $B = 0$. Upon crossing the jet at $n = -5.18 \times 10^{12}$ cm^{-2}, those oscillations become nearly horizontal and almost insensitive to V_t, as if screened, and another series of features appears, dispersing towards the same V_t value that corresponds to the position of the jet. A Fourier transform of the unscreened region (left half of the graph) shows a dominant frequency (f_v) slightly above 1/4 (Fig. 1g), consistent with a fourfold-degenerate annular Fermi surface (Methods). This frequency was nearly constant at large negative n but increased upon crossing the jet, consistent with the simultaneous filling of another conduction-band Fermi pocket. Evidence supporting the interpretation of the jets as the boundary of the dual-surface polarized regime is shown in Supplementary Information Fig. 8.

These observations agree well with the band-structure calculations corresponding to points of the Landau fan on either side of the jet (Fig. 1d), which show fourfold-degenerate isolated valence bands at the Fermi energy on one side and overlapping valence and conduction bands at the Fermi energy on the other. However, we note that our Hartree–Fock calculations do not include the possibility of symmetry-broken states. Within the semimetallic regime, spin- or valley-polarized orders may form, as may a layer-antiferromagnetic order in which opposite-spin bands become layer polarized to the outer surfaces. The screening-derived boundaries in Fig. 1e mark the onset of dual-surface carriers. They do not by themselves distinguish a band-overlapping semimetal from a dual-surface state arising from layer-polarized bands within an interaction-driven phase. Although more detailed calculations will help refine our understanding of the symmetry-broken phases across the (n,D) plane, we expect the boundaries of the dual-surface polarized region to remain roughly unchanged, consistent with the screening behaviour observed when measuring the QOs (see further discussion in Methods).

Superconductivity in semimetallic R8G

We found ten low-resistance pockets within the band-overlapping region, which, as we show below, correspond to the emergence of superconductivity (Fig. 1b,c). Five pockets appear for each sign of D, labelled $SC1_8$ to $SC5_8$ for $D > 0$ (the subscript denotes the total number of graphene layers). We henceforth restrict our focus to the three pockets that appear near $V_b = 0$ ($SC2_8$, $SC3_8$ and $SC4_8$), and we analyse the other two pockets ($SC1_8$ and $SC5_8$) and their $D < 0$ counterparts in Extended Data Figs. 2–4. Figure 2a,b shows detailed ρ_{xx} maps of the region surrounding these pockets, taken at $T = 270$ mK and 8 mK, respectively. Contours of slightly elevated resistance, as seen at higher temperature, developed into three pockets of deeply suppressed ρ_{xx} at the base temperature. Figure 2c,d shows ρ_{xx} versus T and B for the three pockets (taken by sweeping V_b at fixed V_t), which exhibit three dome-like structures consistent with superconductivity. The critical temperatures are small, with $T_c \approx 20$ mK to 170 mK (Fig. 2c and Extended Data Table 1). The corresponding critical fields are similarly low, with B_c of the order of a few millitesla or less. Measurements of dV/dI versus d.c. bias current I_{dc} and B also show distinct nonlinearities characteristic of superconductivity (Extended Data Fig. 3). However, the resistance did not reach zero in any of the five pockets, and dV/dI measurements show unexpected peaks at $I_{dc} = 0$. These peaks are contact-specific and could be eliminated by changing the voltage probes (see further discussion in Methods, Extended Data Fig. 5 and Supplementary Information Fig. 9). Although we do not know its origins, we note that a non-zero saturation of resistance is commonly reported in low-T_c pockets of rhombohedral graphene[7,10–14,33,34].

It is notable that all the superconducting pockets appeared along a nearly fixed value of V_t (V_b) for $D > 0$ ($D < 0$). We speculate that this may have arisen because charge carriers in the normal state resided mainly on the two outer crystal surfaces and were separated by a low-DOS bulk (Fig. 1a). The system thus behaved as two nearly isolated electron gases, held at a common chemical potential by the small fraction of layer-delocalized states. Each gate coupled most strongly to the surface closest to it, with minimal cross-influence due to screening[32], locking features to nearly fixed V_t or V_b rather than along the usual n and D axes. This screening behaviour can be directly understood from the Hartree–Fock band-structure calculations (for example, Fig. 1d), in which the colour scale denotes the average layer polarization of each state. States near the K and K′ points ($k = 0$) predominantly reside on the outer surfaces and can screen their neighbouring gates when populated, whereas states at larger $|k|$ are layer-delocalized and leak across the bulk of the rhombohedral flake. As argued in ref. 32 and Supplementary Information Section II, this spatial structure of the wavefunction naturally gives rise to a single-gate-tracking behaviour, exemplified by the diagonal semimetallic phase boundaries for $n < 0$ in Fig. 1e. In this context, the five pockets of superconductivity apparently correspond to a nearly constant doping of the surface carrying the conduction band and are modulated by doping the valence band, which reside primarily on the opposite surface.

We know of no other material system in which superconductivity forms from such a charge-bifurcated distribution, with valence and conduction bands polarized to opposite surfaces. An open question is whether superconducting gaps form in both the valence and conduction bands simultaneously, and if so, whether the gaps are comparable in magnitude or whether one band instead induces superconductivity

https://doi.org/10.1038/s41567-026-03277-5

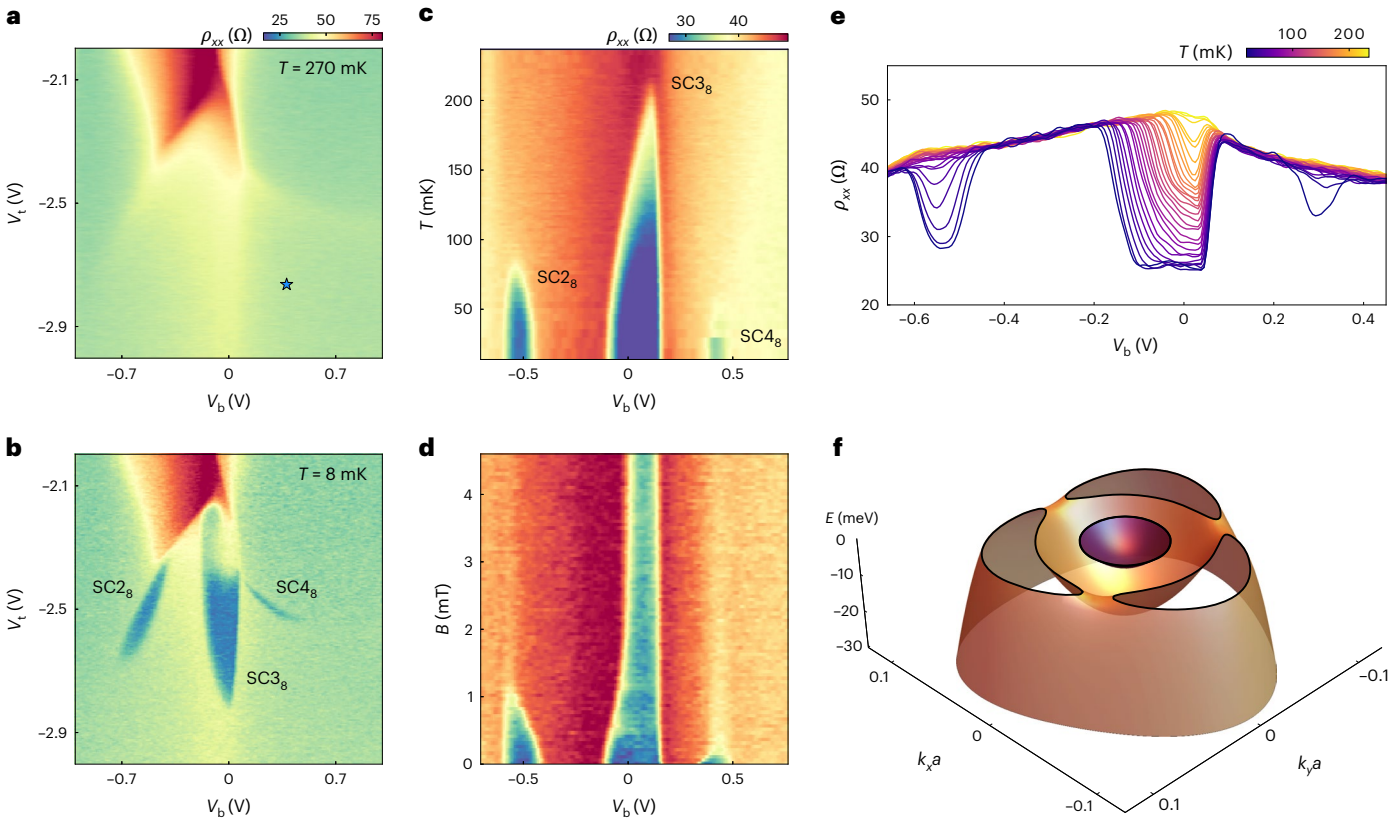

Fig. 2 | Superconductivity in the dual-surface carrier regime of R8G. a, Zoomed-in map of ρ_{xx} versus V_t and V_b at $T = 270$ mK and $B = 0$. **b**, The same map at $T = 8$ mK. **c**, Measurements of ρ_{xx} versus V_b and T at fixed $V_t = -2.55$ V. **d**, Similar measurement versus B. **e**, Line traces of ρ_{xx} versus V_b from **c** at various selected T. **f**, Calculated Hartree–Fock band structure, E versus k_x and k_y, at $n = -1.96 \times 10^{12}$ cm^{-2} and $D = 0.203$ V nm^{-1} corresponding to the position of the blue star in **a**. The conduction (valence) band is shown in purple (orange). The Fermi surface is denoted at $E_F = 0$ with a solid black outline.

in the other through a proximity effect. At minimum, the gate-tracking characteristics described above indicate that both bands play a role in the superconductivity. This observation invites considerations of how the extended spatial distribution of the wavefunction is manifest in attempts to theoretically describe pairing in this system. Our band-structure calculations are especially noteworthy for values of n and D around where SC2$_8$, SC3$_8$ and SC4$_8$ appear, in which a local maximum in the DOS coincides with a Lifshitz transition in the valence band and a small simply-connected Fermi pocket from the conduction band (Figs. 1e and 2f). We emphasize the distinction from other crystalline graphene systems, where superconductivity likewise tracks features potentially associated with a high DOS but without the extra interplay provided by the charge-delocalized semimetallic normal state. Further work will be needed to understand which features of each band promote superconductivity.

Superconductivity in a moiré R7G sample

The complementary role of layer-polarized conduction and valence bands in inducing superconductivity is even more clear in measurements of a sample of rhombohedral heptalayer graphene (R7G) that is aligned with hBN to give a 13.5-nm moiré superlattice. Figure 3a is a map of ρ_{xx} as a function of V_b and V_t for the R7G sample at $B = 0$. Key features are summarized schematically in the inset. Compared with the misaligned R8G device, this sample lacked the correlated insulator and symmetry-broken metal near $n = D = 0$, but at larger D, it developed correlated insulating states at commensurate fillings ν of the moiré conduction band (Extended Data Fig. 1). We observed two distinct superconducting pockets (SC1$_7$ and SC2$_7$) emerging out of a sharp resistance bump feature that tracked fixed V_t (shown in light blue in the schematic in Fig. 3a). The more robust pocket, SC1$_7$, is bounded by two perpendicular bumps that closely track fixed V_b (Fig. 3b and Extended Data Fig. 6). This bounding is like the features associated with the SC5$_8$ pocket in the R8G sample (Extended Data Fig. 7). The weaker pocket, SC2$_7$, is also directly connected to a perpendicular resistance bump. Both SC1$_7$ and SC2$_7$ lay within the band-overlapping regime, as determined by our analysis of Landau fans taken across the jet emerging from the large-D insulating state at the CNP (Fig. 3c; further data and analysis in Methods, Extended Data Fig. 8 and Supplementary Information Fig. 6). In particular, in Fig. 3c we see a dispersing sequence of QOs with $f_\nu = 1/4$ for $V_t \lesssim -4.75$ V and screening of those QOs with a corresponding rapid increase of f_ν for $V_t \gtrsim -4.75$ V, indicating that the jet from the CNP defines the band-overlapping to band-isolated region, analogous to the behaviour seen in the R8G sample.

Figure 3d,e shows measurements of ρ_{xx} for SC1$_7$ versus T and B as V_t is swept at fixed $V_b = 1.40$ V. Both exhibit characteristic domes like those seen in R8G. Figure 3f displays line traces of ρ_{xx} versus V_t for several selected T. There was a small bump in the resistance at higher T, which developed into a deep suppression of ρ_{xx} at the base temperature. The measured ρ_{xx} versus T shown in the left inset highlights the abrupt downturn of the resistance below approximately 90 millikelvin, before it saturated near 20 Ω. The dV/dI measurements in the right inset of Fig. 3f provide further evidence for superconductivity, as there were sharp peaks at a critical current of approximately 15 nanoamperes and a recovery of nearly linear transport above B_c. Analogous measurements for SC2$_7$ are shown in Extended Data Fig. 9.

The ρ_{xx} bump that developed into the two superconducting pockets in R7G clearly seems to be a feature of the conduction band, as

https://doi.org/10.1038/s41567-026-03277-5

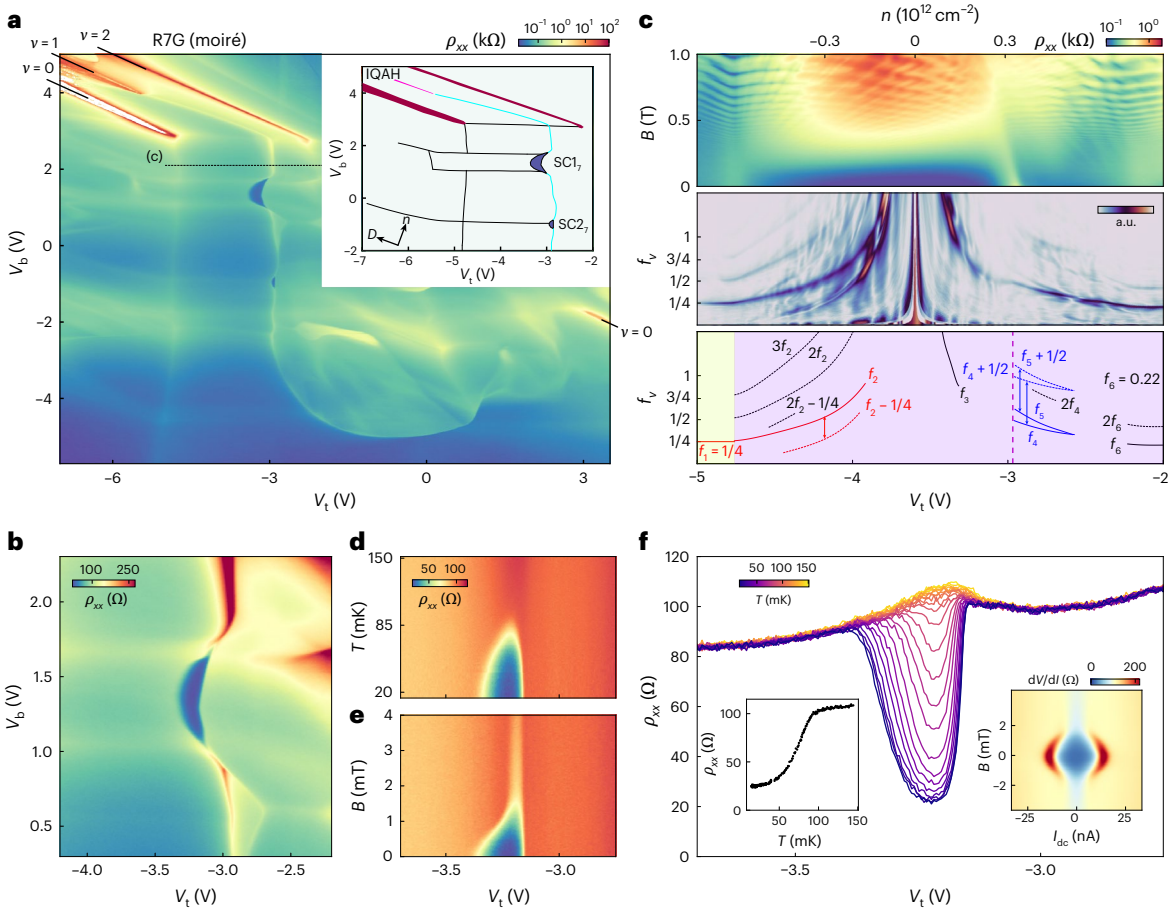

Fig. 3 | Superconductivity in a moiré R7G device. a, Map of ρ_{xx} versus V_t and V_b taken at the base temperature and $B = 0$. Inset: schematic denoting some of the key transport features. Trivial (Chern) insulators at integer ν are shown in red (pink). Black and blue curves denote resistance bump features. Dark blue pockets correspond to superconductivity. **b**, Zoomed-in map of ρ_{xx} around the region of $SC1_7$. **c**, Top: Landau fan taken by sweeping V_t at fixed $V_b = 2.1$ V along the black dashed line in **a**. Middle: Fourier transform of the Landau fan. Bottom: schematic denoting the dominant frequencies seen in the FFT. Background colours denote the band-isolated (yellow) and band-overlapping regions (purple). **d**, Measurements of ρ_{xx} versus V_t and T at fixed $V_b = 1.4$ V. **e**, Similar measurement versus B. **f**, Line traces of ρ_{xx} at various selected T. Left inset: measurement of ρ_{xx} versus T. Right inset: measurement of dV/dI versus I_{dc} and B. Measurements in both insets were taken at the optimal doping of $SC1_7$ ($V_t = -3.22$ V and $V_b = 1.4$ V).

it persisted into the electron-doped region ($n > 0$) at large D when a gap opened at the CNP and because its trajectory became nearly independent of V_b within the dual-surface regime due to screening from coexisting valence band states on the bottom surface. A detailed analysis of the QOs in Landau fan measurements across the bump feature indicated that it separated an isospin-unpolarized metal to the left from a spin-polarized half-metal to the right (Fig. 3c), although alternative interpretations remain possible (Methods). The resistive bump shifted to more negative V_t with increasing B (Fig. 3c), consistent with a spin-polarized state to the right gaining Zeeman energy over the unpolarized state to the left.

In this picture, $SC1_7$ is associated with electrons in the conduction band, lies on the boundary between isospin-unpolarized and isospin-polarized states, and is turned on and off by valence band features from the opposite crystal surface. Indeed, in-plane field measurements of the superconductivity indicate spin-polarized ordering[35]. $SC2_7$ shares similar characteristics. Both pockets appeared only when conduction band states were polarized away from the moiré interface (with the hBN aligned to the bottom surface), indicating that superconductivity is disfavoured when these states are moiré-adjacent. These conclusions are supported by our self-consistent Hartree–Fock simulations, which show that the presence of a moiré superlattice disfavours the charge-separated semimetal for displacement fields polarizing the conduction band towards the moiré interface (see Supplementary Information Section II for a further discussion).

Chern insulator at large displacement field

Last, we show that the same conduction-band feature that hosts superconductivity in the semimetallic region of the moiré R7G device also hosts an IQAH state once the bands are separated, with quantization of the Hall resistance to $\rho_{xy} = \pm h/e^2$. Upon increasing D and exiting the semimetallic regime, the resistance bump abruptly became responsive to both V_t and V_b, consistent with a disappearance of valence-band-mediated screening from the remote gate. Figure 4a,b shows two-dimensional scans along the n and D axes corresponding to the top left corner of Fig. 3a. These scans show the evolution of the resistive bump into an IQAH state when it drifts to $\nu \approx 1$ at $D \gtrsim 0.58$ V nm^{-1}. The IQAH state is marked by the simultaneous suppression of ρ_{xx} towards zero (Fig. 4a,e) and quantization of $|\rho_{xy}|$ to h/e^2 (Fig. 4b,e). In a Landau fan (Fig. 4c,d), the relevant ρ_{xx} and ρ_{xy} featured a slope with a trajectory consistent with $C = +1$ under the Středa formula and persisted to at least 8 T. Other sweeps taken at $\nu = 1.06$ while cycling B (Fig. 4f) show a single hysteresis loop with ρ_{xy} switching between $\pm h/e^2$, which provides definitive evidence for the $|C| = 1$ IQAH state. The appearance of a IQAH state with Chern number $C = 1$ at high D is in

https://doi.org/10.1038/s41567-026-03277-5

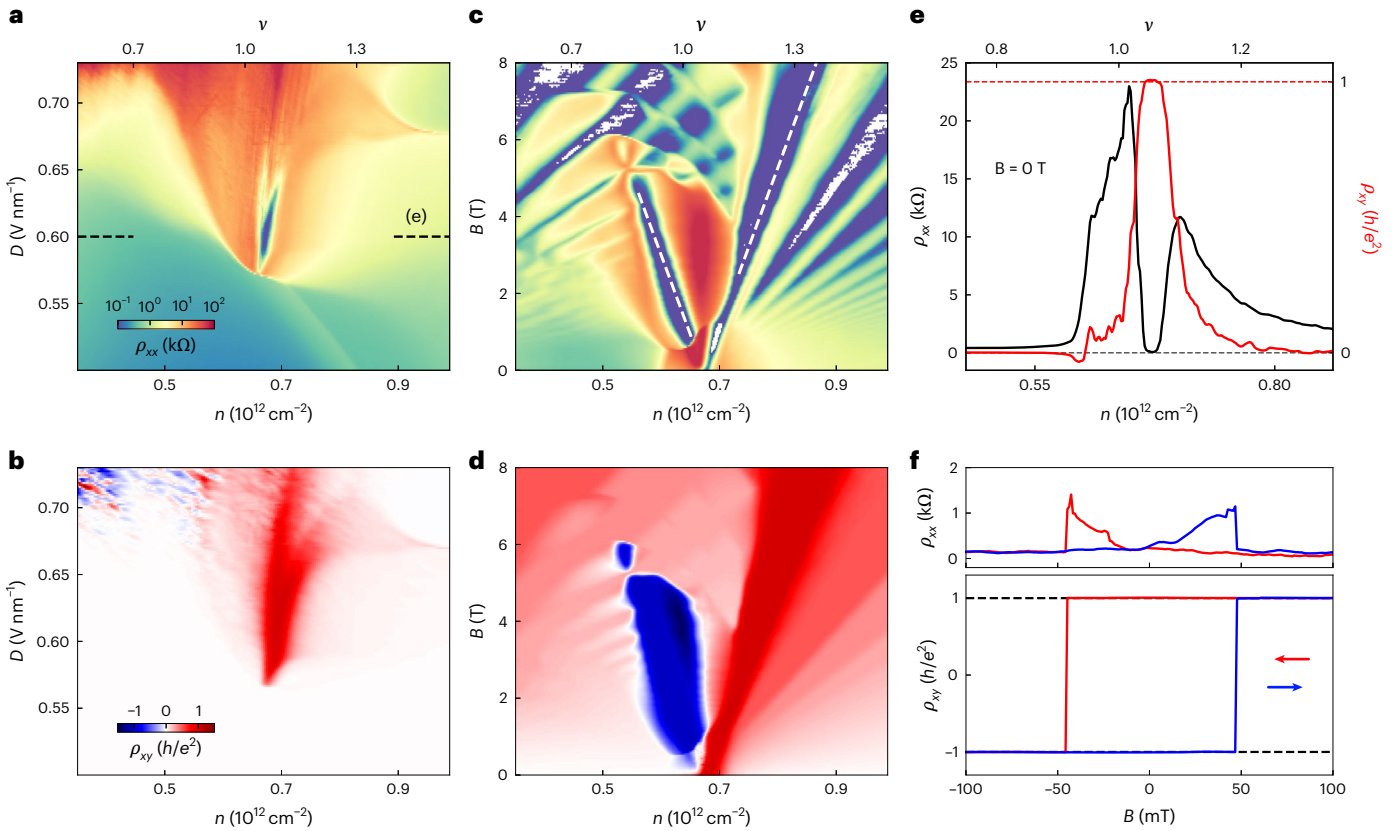

Fig. 4 | IQAH state near $\nu = 1$ in the moiré R7G device. a, Map of ρ_{xx} versus ν and D at $B = 0$. **b**, Similar map of ρ_{xy} antisymmetrized at $|B| = 100$ mT. **c**, Landau fan of ρ_{xx} taken at $D = 0.60$ V nm^{-1} (marked by the dashed lines in **a**). White dashed lines indicate the Středa trajectories of the $C = +1$ and -1 states. White colours indicate negative measured resistances. **d**, Same as **c** but for ρ_{xy}. Landau fans are symmetrized (**c**) and antisymmetrized (**d**). **e**, Line traces of ρ_{xx} (black) and ρ_{xy} (red) versus ν at $B = 0$ and $D = 0.60$ V nm^{-1}. **f**, Measured ρ_{xx} and ρ_{xy} as B is cycled at $\nu = 1.06$ and $D = 0.60$ V nm^{-1}. **a** and **e** were taken at $T = 9$ mK. All other measurements were taken at $T = 100$ mK.

line with previous measurements on four- to ten-layer rhombohedral graphene[22–25,36].

Two features in Fig. 4 extend beyond conventional IQAH phenomenology. First, the Chern insulator was apparently not pinned exactly to $\nu = 1$ (Extended Data Fig. 10). In fact, all the correlated insulators on the moiré-remote side shifted progressively away from integer ν as D was increased (Supplementary Information Fig. 4), underscoring the need to clarify the experimental conditions for opening many-body gaps in thicker rhombohedral samples. By contrast, the correlated insulators on the moiré-adjacent side did not exhibit this behaviour. Second, the Landau fan revealed another $C = -1$ state that emerged abruptly for $B \gtrsim 0.6$ T, like behaviour recently reported in moiré rhombohedral hexalayer graphene[36] and twisted bilayer-trilayer graphene[37].

Discussion

Superconductivity appears widely across crystalline graphene multilayers, but it is unclear whether the underlying pairing mechanism is universal. The unusual charge-delocalized semimetallic normal state that we identified introduces a theoretical scenario in which two spatially separated electronic reservoirs can interact to reshape the effective pairing interaction. Gate-tracking behaviour in both R8G and moiré R7G indicates that superconductivity is primarily tied to features in the conduction band, indicating that the valence band plays a secondary—yet still important—role. Regardless of the pairing mechanism, superconductivity requires an attractive interaction to overcome the renormalized Coulomb repulsion. Within the Tolmachev–Anderson–Morel framework for phonon-mediated superconductivity[38,39], other carriers in the valence band could enhance screening and thereby strengthen the pairing. Alternatively, the charge-separated geometry resembles 'synthetic' electronic pairing proposals[40–46] in which one charge layer mediates an effective attraction in another (for example, dynamical, excitonic or Kohn–Luttinger scenarios). Furthermore, the propensity of crystalline graphene systems for symmetry-breaking necessitates consideration of pairing arising from fluctuations in the isospin degrees of freedom[47], in which screening from the extra charge layer would naively suppress Coulomb-driven pairing; however, careful consideration is required.

Estimates of the superconducting coherence length, mean free path and Fermi wavevectors place the system in the clean, weak-coupling limit, although extracting these parameters is complicated by the coexistence of valence- and conduction-band carriers (Methods and Extended Data Table 1). If confirmed, this regime renders the pairing problem in rhombohedral graphene particularly amenable to controlled theoretical treatments. Future experiments tracking the evolution of superconductivity in the semimetallic regime as a function of the layer number will probably be helpful for unravelling its nature. A recent study of rhombohedral hexalayer graphene revealed superconductivity in a similar region of parameter space as the $SC3_8$ pocket[15]; our measurements extend the presence of superconductivity beyond six-layer samples, motivating the possibility that it persists into the regime of bulk rhombohedral graphite. Thicker flakes are of particular interest because the larger spatial separation of the two surfaces could further modify the presence and strength of the superconductivity.

Taken together, our findings raise questions about superconductivity in graphene multilayers, in which the highly non-uniform charge distribution along the stacking axis seems to play a key role in pairing. They also reveal intriguing connections between superconductivity and topological many-body phases in moiré superlattices. The

evolution of a sharp resistive bump feature from a superconducting state at low D into an IQAH state at higher D in moiré R7G highlights the versatility of this platform for studying the interplay between superconductivity and topology.

Online content

Any methods, additional references, Nature Portfolio reporting summaries, source data, extended data, supplementary information, acknowledgements, peer review information; details of author contributions and competing interests; and statements of data and code availability are available at https://doi.org/10.1038/s41567-026-03277-5.

References

1. Xiao, R. et al. Density functional investigation of rhombohedral stacks of graphene: topological surface states, nonlinear dielectric response, and bulk limit. *Phys. Rev. B* **84**, 165404 (2011).
2. Guinea, F., Castro Neto, A. H. & Peres, N. M. R. Electronic states and Landau levels in graphene stacks. *Phys. Rev. B* **73**, 245426 (2006).
3. Min, H. & MacDonald, A. H. Chiral decomposition in the electronic structure of graphene multilayers. *Phys. Rev. B* **77**, 155416 (2008).
4. Koshino, M. & McCann, E. Trigonal warping and Berry's phase $n\pi$ in ABC-stacked multilayer graphene. *Phys. Rev. B* **80**, 165409 (2009).
5. Slizovskiy, S., McCann, E., Koshino, M. & Fal'ko, V. I. Films of rhombohedral graphite as two-dimensional topological semimetals. *Commun. Phys.* **2**, 164 (2019).
6. Shi, Y. et al. Electronic phase separation in multilayer rhombohedral graphite. *Nature* **584**, 210–214 (2020).
7. Zhou, H., Xie, T., Taniguchi, T., Watanabe, K. & Young, A. F. Superconductivity in rhombohedral trilayer graphene. *Nature* **598**, 434–438 (2021).
8. Zhou, H. et al. Isospin magnetism and spin-polarized superconductivity in Bernal bilayer graphene. *Science* **375**, 774–778 (2022).
9. Zhang, Y. et al. Enhanced superconductivity in spin-orbit proximitized bilayer graphene. *Nature* **613**, 268–273 (2023).
10. Holleis, L. et al. Nematicity and orbital depairing in superconducting Bernal bilayer graphene. *Nat. Phys.* **21**, 444–450 (2025).
11. Patterson, C. L. et al. Superconductivity and spin canting in spin–orbit-coupled trilayer graphene. *Nature* **641**, 632–638 (2025).
12. Choi, Y. et al. Superconductivity and quantized anomalous Hall effect in rhombohedral graphene. *Nature* **639**, 342–347 (2025).
13. Zhang, Y. et al. Twist-programmable superconductivity in spin–orbit-coupled bilayer graphene. *Nature* **641**, 625–631 (2025).
14. Yang, J. et al. Impact of spin–orbit coupling on superconductivity in rhombohedral graphene. *Nat. Mater.* **24**, 1058–1065 (2025).
15. Qin, P. et al. Extreme anisotropy in the metallic and superconducting phases of rhombohedral hexalayer graphene. Preprint at https://arxiv.org/abs/2504.05129v4 (2025).
16. Li, C. et al. Tunable superconductivity in electron- and hole-doped Bernal bilayer graphene. *Nature* **631**, 300–306 (2024).
17. Han, T. et al. Signatures of chiral superconductivity in rhombohedral graphene. *Nature* **643**, 654–661 (2025).
18. Zhou, H. et al. Half- and quarter-metals in rhombohedral trilayer graphene. *Nature* **598**, 429–433 (2021).
19. Han, T. et al. Correlated insulator and Chern insulators in pentalayer rhombohedral-stacked graphene. *Nat. Nanotechnol.* **19**, 181–187 (2024).
20. Liu, K. et al. Spontaneous broken-symmetry insulator and metals in tetralayer rhombohedral graphene. *Nat. Nanotechnol.* **19**, 188–195 (2024).
21. Zhou, W. et al. Layer-polarized ferromagnetism in rhombohedral multilayer graphene. *Nat. Commun.* **15**, 2597 (2024).
22. Lu, Z. et al. Fractional quantum anomalous Hall effect in multilayer graphene. *Nature* **626**, 759–764 (2024).
23. Lu, Z. et al. Extended quantum anomalous Hall states in graphene/hBN moiré superlattices. *Nature* **637**, 1090–1095 (2025).
24. Waters, D. et al. Chern insulators at integer and fractional filling in moiré pentalayer graphene. *Phys. Rev. X* **15**, 011045 (2025).
25. Xie, J. et al. Tunable fractional Chern insulators in rhombohedral graphene superlattices. *Nat. Mater.* **24**, 1042–1048 (2025).
26. Ding, J. et al. Electric-field switchable chirality in rhombohedral graphene Chern insulators stabilized by tungsten diselenide. *Phys. Rev. X* **15**, 011052 (2025).
27. Su, W. P., Schrieffer, J. R. & Heeger, A. J. Solitons in polyacetylene. *Phys. Rev. Lett.* **42**, 1698–1701 (1979).
28. Myhro, K. et al. Large tunable intrinsic gap in rhombohedral-stacked tetralayer graphene at half filling. *2D Mater.* **5**, 045013 (2018).
29. Zhang, F., Jung, J., Fiete, G. A., Niu, Q. & MacDonald, A. H. Spontaneous quantum Hall states in chirally stacked few-layer graphene systems. *Phys. Rev. Lett.* **106**, 156801 (2011).
30. Velasco Jr, J. et al. Transport spectroscopy of symmetry-broken insulating states in bilayer graphene. *Nat. Nanotechnol.* **7**, 155–160 (2012).
31. Han, T. et al. Orbital multiferroicity in pentalayer rhombohedral graphene. *Nature* **623**, 41–47 (2023).
32. Kolář, K. et al. Single-gate tracking behavior in flat-band multilayer graphene devices. *Phys. Rev. B* **113**, 075131 (2026).
33. Deng, J. et al. Superconductivity and ferroelectric orbital magnetism in semimetallic rhombohedral hexalayer graphene. Preprint at http://arxiv.org/abs/2508.15909 (2025).
34. Seo, J. et al. Family of unconventional superconductivities in crystalline graphene. Preprint at http://arxiv.org/abs/2509.03295 (2025).
35. Kumar, M. et al. Pervasive spin-triplet superconductivity in rhombohedral graphene. Preprint at http://arxiv.org/abs/2511.16578 (2025).
36. Xie, J. et al. Unconventional orbital magnetism in graphene-based fractional Chern insulators. Preprint at http://arxiv.org/abs/2506.01485 (2025).
37. Su, R. et al. Moiré-driven topological electronic crystals in twisted graphene. *Nature* **637**, 1084–1089 (2025).
38. Tolmachev, V. V. Logarithmic criterion for superconductivity. *Dokl. Akad. Nauk SSSR* **140**, 563–566 (1961).
39. Morel, P. & Anderson, P. W. Calculation of the superconducting state parameters with retarded electron–phonon interaction. *Phys. Rev.* **125**, 1263–1271 (1962).
40. Little, W. A. Possibility of synthesizing an organic superconductor. *Phys. Rev.* **134**, A1416–A1424 (1964).
41. Ginzburg, V. On surface superconductivity. *Phys. Lett.* **13**, 101–102 (1964).
42. Allender, D., Bray, J. & Bardeen, J. Model for an exciton mechanism of superconductivity. *Phys. Rev. B* **7**, 1020–1029 (1973).
43. Malozovsky, Y. M. & Fan, J. D. The metal - insulator phase transition, quasiparticle damping and superconductivity in a layered Fermi gas. *Supercond. Sci. Technol.* **9**, 622–638 (1996).
44. Hamo, A. et al. Electron attraction mediated by Coulomb repulsion. *Nature* **535**, 395–400 (2016).
45. Fatemi, V. & Ruhman, J. Synthesizing Coulombic superconductivity in van der Waals bilayers. *Phys. Rev. B* **98**, 094517 (2018).
46. Chubukov, A. V. & Kivelson, S. A. Superconductivity in engineered two-dimensional electron gases. *Phys. Rev. B* **96**, 174514 (2017).
47. Scalapino, D. J. A common thread: the pairing interaction for unconventional superconductors. *Rev. Mod. Phys.* **84**, 1383–1417 (2012).

Methods

Device fabrication

We first identified regions of probable rhombohedral stacking within flakes of exfoliated graphene using an infrared camera mounted on an optical microscope. We then mapped the stacking domains in detail with amplitude-modulated Kelvin probe force microscopy using an atomic force microscope (Bruker Icon) with an SCM-PIT-V2 tip[24]. The rhombohedral region of interest was subsequently isolated using a resist-free local-anodic-oxidation nanolithography process[48]. To create the van der Waals heterostructure, we first prepared the bottom portion of the stack by picking up an hBN and graphite dielectric/back gate and placing them onto an SiO_2 substrate. We then cleaned the surface of the hBN using contact-mode atomic force microscopy (using an OTESPA-R3 atomic force microscope tip and a line spacing of ~100 nm). We separately prepared the top half of the stack, consisting of graphite/hBN/rhombohedral graphene, and deposited it onto the back half. We used standard dry-transfer techniques with a polycarbonate film on a polydimethylsiloxane stamp for all van der Waals assembly. For the moiré R7G sample, the straight edges of the rhombohedral-graphene flake were aligned to those of the hBN.

After stacking, standard device fabrication procedures were employed to create the dual-gated Hall bar device (reactive-ion etching and evaporation of 7/70 nm of Cr/Au, all using poly(methyl methacrylate) masks patterned by electron-beam lithography). Extended Data Fig. 1 shows optical micrographs of the completed devices.

Transport measurements

Transport measurements were carried out in a dilution refrigerator (Bluefors XLD) with a one-axis superconducting magnet. Both devices were subsequently measured in a dilution refrigerator (Bluefors LD) equipped with a three-axis superconducting vector magnet. Unless otherwise specified, measurements were carried out at the nominal base mixing chamber temperature of the fridge ($T = 8$ mK, as measured by a factory-supplied RuO_x sensor). Four-terminal lock-in measurements were performed by sourcing a small alternating current between $I_{ac} = 100$ pA and 6.67 nA at a frequency <40 Hz, which was chosen to accurately capture sensitive transport features while minimizing electronic noise. The reported resistances may have a systematic uncertainty of a few per cent owing to the different voltage-divider configurations used to add a d.c. bias. When measuring the IQAH state, we calibrated the current more precisely to minimize this error. All ρ_{xx} and dV/dI measurements are presented after multiplying the raw measured resistance values by the aspect ratio W/L, set by the width W and length L of the portion of the Hall bar between the voltage probes. In addition, a global bottom-gate voltage between −20 V and +20 V was applied to the Si substrate to improve the contact resistance. The silicon gate voltage was adjusted between different portions of the map shown in Fig. 1b, resulting in the artificial boundaries indicated by the black arrows.

The charge carrier density n and the out-of-plane electric displacement field D were defined according to $n = (C_b V_b + C_t V_t)/e$ and $D = (C_b V_b - C_t V_t)/2\epsilon_0$, where C_t and C_b are the top- and bottom-gate capacitance per unit area and ϵ_0 is the vacuum permittivity. C_t and C_b were estimated by fitting the slopes of the quantum Hall states in the Landau fan diagrams. We note that our definition of D has the opposite sign convention from standard electrostatics, such that the IQAH state in the R7G device appears at $D > 0$, as is common in the literature.

In some Landau fan diagrams, we symmetrized ρ_{xx} and antisymmetrized ρ_{xy} to reduce the effects of geometric mixing following the relations $\rho_{xx} = (\rho_{xx}(B > 0) + \rho_{xx}(B < 0))/2$ and $\rho_{xy} = (\rho_{xy}(B > 0) - \rho_{xy}(B < 0))/2$. In measurements of superconductivity versus B, we adjusted the nominal value of B by a few millitesla such that the ρ_{xx} data were symmetric about $B = 0$, which was necessary due to the small, trapped flux in the superconducting magnet coil.

The two-terminal resistance of all the contacts used in the measurements of $SC1_7$ and $SC2_7$ in the moiré-R7G device was between 4 kΩ and 10.2 kΩ, and it exhibited a linear response over the range of a.c. and d.c. biases applied. For the R8G device, the measurement of the contact resistance was complicated by the insulator at $n = D = 0$, and therefore, we do not have reliable values to report. The upper bound is 262 kΩ, but we caution that the true values are very probably much lower.

Layer number determination

To determine the number of graphene layers in the misaligned sample, we examined a Landau fan at $D = 0$ (Supplementary Information Fig. 1). As explained in detail in ref. 6, at high B the most robust Landau level gap corresponds to a filling factor $\nu_{LL} = -2N$, where N is the number of graphene layers. In the misaligned sample, we found that the most robust filling factor $\nu_{LL} = -16$, thus providing an unambiguous identification of the flake as having eight layers.

In the moiré sample, the added complexity in the band structure precluded the application of this technique. In thinner samples, there is additionally a magnetic-field-driven Chern insulator state arising from the CNP, which can be used to determine the layer number[24]. However, we found that in thicker moiré samples, such a state does not apparently arise. Thus, we relied on the optical contrast to determine the layer number. Supplementary Information Fig. 2 shows an optical micrograph of the flake. By carefully counting monolayer and bilayer steps in the graphene flake, as indicated by the changes in their optical contrast, we clearly identified this flake as having seven layers.

Determination of moiré period and twist angle

To extract the moiré wavelength in the aligned R7G device, we fitted the sequence of Brown–Zak magnetoconductance oscillations extracted from a Landau fan. Supplementary Information Fig. 3 shows an example, taken at $D = 0.5$ V nm^{-1}, although we confirmed the fit with several more fans. To highlight Brown–Zak oscillations, we plotted the average conductance $\langle G_{xx} \rangle$ over the entire measured range of density versus B. This averaging scheme suppressed the effect of dispersing quantum Hall states. The Brown–Zak oscillations occurred when $\phi/\phi_0 = 4B/n_s\phi_0 = p/q$, where ϕ is the magnetic flux through the moire unit cell, $\phi_0 = h/e$ is the magnetic flux quantum and p and q are integers. We extracted the superlattice density $n_s = 2.55 \times 10^{12}$ cm^{-2} from a best fit of all the magnetoconductance peaks. This value is consistent with the positions of the insulating states seen on the moiré-adjacent side at integer moiré band fillings (Supplementary Information Fig. 4c,d).

The moiré band filling factor ν was defined according to $\nu = n/(n_s/4)$. The superlattice density is related to the moiré wavelength by $L_M = \sqrt{8/\sqrt{3}n_s} = 13.5$ nm. We then found the twist angle, $\theta = 0.42°$, from the equation

$$L_M(\theta, a, \delta_a) = \frac{(1+\delta_a)a}{\sqrt{2(1+\delta_a)(1-\cos\theta)+\delta_a^2}},$$

where $a = 0.246$ nm is the lattice constant of graphene, θ is the twist angle between the hBN and the rhombohedral graphene, and $\delta_a = \frac{a_{hBN}-a}{a} \approx 0.017$ is the lattice mismatch between the lattice constants of the hBN (a_{hBN}) and graphene. We note that the conversion to twist angle depends on the choice of the lattice mismatch between graphene and hBN, which is not precisely known.

Key parameters of the superconducting states

Extended Data table 1 provides simple estimates for some of the key quantities associated with superconductivity: critical temperature T_c, critical out-of-plane field B_c and superconducting coherence length ξ. To estimate T_c, we fitted a line to the measured ρ_{xx} in the normal state just above the abrupt downturn. We then estimated T_c as the temperature at which ρ_{xx} falls to 90% of this value. We used a similar procedure

for determining B_c from measurements of ρ_{xx} versus B. We estimated the superconducting coherence length as $\xi = \sqrt{\Phi_0/(2\pi B_c)}$, where Φ_0 is the superconducting magnetic flux quantum.

To further assess the nature of superconductivity, we attempted to provide simple estimates for the mean free path in the normal state ℓ_{mf} and the relevant Fermi wavevector k_F. The ratio ξ/ℓ_{mf} parameterizes the disorder strength, where values much less than unity are generally required to support exotic order parameters. The ratio $k_F\xi$ provides insight into whether pairing is in the strong- or weak-coupling limit, with values much larger than unity signalling BCS-like (weak-coupling) behaviour. We provide rough estimates of these values here, but caution that the semimetallic nature of the normal state complicates their extraction, as we do not have a direct measurement of the relative densities and mobilities of the valence- and conduction-band carriers. To estimate ℓ_{mf}, we assessed the lowest magnetic field at which QOs first appeared. This roughly corresponds to the condition in which the mean free path is equal to the circumference of a cyclotron orbit: $\ell_{mf} \approx 2\pi k_F \ell_B^2$, where k_F is the Fermi wavevector and ℓ_B is the magnetic length. The Fermi wavevector can be calculated as $k_F = \sqrt{4\pi f\,|n|}$.

The primary complication is that each band has a different Fermi wavevector and, potentially, a different f_ν, and we do not have independent experimental measures of each of them when they coexist at the Fermi level, nor do we know for certain whether to use the value from the conduction or valence band in our estimates. As a starting point, we assumed that the superconductivity was driven by the conduction band and estimated k_F from our calculations for R8G. The region where we observed the most robust superconductivity in R8G corresponds to $k_F \approx 0.15\ \mathrm{nm}^{-1}$ in the conduction band (estimated from extrapolating the conduction-band Fermi surface from the theoretical calculation presented in Fig. 2f). As the onset of QOs was at $B \approx 400$ mT in the Landau fans, we roughly estimated $\ell_{mf} \approx 1.5$ µm. Following this, $\xi/\ell_{mf} \approx 0.4$ and $k_F\xi \approx 100$, nominally corresponding to the clean limit of weakly coupled superconductivity.

Superconductivity in R8G at $D < 0$

Extended Data Fig. 4 shows zoomed-in transport measurements of the five superconducting pockets in R8G at $D < 0$, which we label $SC6_8$ through $SC10_8$. Overall, they seem to very closely resemble the corresponding $SC1_8$–$SC5_8$ pockets. One noteworthy difference is the region of elevated ρ_{xx} at negative n and D, which does not have an associated counterpart for $D > 0$. Presently, we do not understand this feature or why it appears only for one sign of D. Another difference is that the $SC10_8$ pocket is much more extended than its corresponding $SC5_8$, nearly connecting with $SC9_8$. This behaviour indicates that the $SC9_8$ and $SC10_8$ pockets (and, similarly, $SC4_8$ and $SC5_8$ for the other sign of D) are, in fact, one contiguous pocket, with T_c just below our base temperature in between the two.

Interpretation of screening boundaries

In both devices, the screening-derived boundaries in the n–D plane were used operationally to mark the onset of dual-surface carriers. On their own, these boundaries do not distinguish whether the two surfaces originated from a conduction–valence overlap (a semimetal in the band-structure sense) or from two layer-polarized bands within an interaction-driven phase (for example, within a layer-antiferromagnetic framework). We, therefore, use the term 'semimetallic' as an interpretation of the carrier origin, while keeping this caveat explicit.

For the moiré R7G device, we considered the conduction–valence overlap interpretation to be the most compelling. We did not observe in this sample a layer-antiferromagnetic insulator near $n = D = 0$, so a dual-surface configuration arising from such an interaction-driven surface splitting is not indicated experimentally. Instead, the onset of dual-surface screening occurred in the regime where our calculations show overlapping valence and conduction bands at the Fermi energy, which naturally yields two oppositely layer-polarized surfaces.

For the misaligned R8G device, two interpretations remain possible. Dual-surface carriers could arise either from an interaction-driven reconstruction within a valence-band manifold that produces two layer-polarized Fermi surfaces or from a conduction–valence overlap within a phase that may also be spin or valley polarized. Although we do not have definitive evidence that excludes the former scenario, the smooth connection of the screening boundaries to the region where the calculations indicate a band overlap makes the semimetallic interpretation probable in practice. Furthermore, the elevated-resistance features associated with the insulating state at $n = D = 0$ seem to lie entirely within the screening boundaries. For these reasons, we adopt the 'semimetallic' terminology in the main text, while emphasizing that the screening boundaries themselves should be read as the onset of dual-surface transport rather than as a unique diagnostic of band overlap.

Transport anomalies associated with the superconducting states

Several transport features associated with the superconducting pockets in the R7G and R8G devices were not anticipated for standard superconductors. First, the resistance did not reach zero in any of the pockets we studied. Instead, it saturated at a value below 100 Ω. As mentioned earlier, this is seen routinely in thinner crystalline graphene superconductors[7,10–14,33,34]. Second, for many of the pockets, the resistance above B_c remains lower than at nearby gate voltages (see Extended Data Fig. 5 for an analysis of $SC3_8$). In the same regime, there is also remnant nonlinearity in the dV/dI versus I_{dc} measurements. This was also seen in previous reports on thinner graphene[10,12]. Linear transport eventually recovers at larger B. Third, in R8G there is an unexpected zero-bias peak in the dV/dI versus I_{dc} measurements, which extends far above B_c and has no apparent association with the superconductivity. We found that this anomaly is contact-specific and did not appear in similar measurements taken with other voltage probes (Extended Data Fig. 5a,b.)

We do not know the origins of these features and so speculate on some possibilities. One possible origin of the non-zero resistance is resistive heating at the contacts. Several junctions formed between differently gated regions near the metal electrodes, and given the very low T_c, even modest heating could potentially result in some non-zero resistance. The zero-bias peak in the R8G device may also have resulted from contact imperfections. As for the unusual transport features above B_c, they may be related to a competing many-body state that emerged with the suppression of superconductivity. Given that superconductivity formed along a sharp resistance bump, a possibility is that this resistive state emerged above B_c and also exhibited nonlinearity. Further work will be needed to better understand these observations.

Notably, the non-zero saturation in our samples did not seem to arise from an unexpectedly high electron temperature. For example, the resistance drop of the $SC4_8$ pocket began below 50 mK and persisted down to the nominal base temperature of the fridge, whereas the neighbouring $SC3_8$ pocket exhibited unexpected resistance saturation at comparable temperatures (Fig. 3e). Similarly, Extended Data Fig. 9c shows that the edges of the $SC2_7$ dome also continued to develop down to at least 20 mK. In fact, non-zero-resistance saturation at the base temperature has been reported previously in many different superconductors, collectively referred to as 'anomalous metals' or 'failed superconductors'[49]. At present, there is no compelling theory to describe this behaviour. Given that several groups have reported similar non-zero resistance in rhombohedral graphene[7,10–14], we also consider the possibility that this behaviour is fundamental.

Despite the finite saturation resistance, we observe signatures of Fraunhofer oscillations in ρ_{xx} maps versus V_b and $B_\perp$

(Extended Data Fig. 5d,e), which are hallmarks of phase-coherent Josephson transport. The oscillation period ΔB sets an effective junction area $A_{\mathrm{eff}} \approx \Phi_0/\Delta B = 3.4\ \mu\mathrm{m}^2$, and the lobe structure of $I_c(B_\perp)$ (where I_c is the critical current of the superconducting state) is consistent with interference through a spatially extended weak link. The weak-link area is roughly comparable with the area between the voltage probes, indicating that the strength of the superconductivity is spatially inhomogeneous. Together, these features establish superconducting phase coherence even when a small residual resistance is present.

Fermiology analysis

To extract information about the Fermi surfaces, we applied fast Fourier transforms (FFTs) of $\rho_{xx}(1/B)$ to the Landau fans shown in Figs. 1f and 3c, Extended Data Fig. 8, and Supplementary Information Figs. 5 and 7. FFTs were taken after first subtracting a fifth-order polynomial from the raw longitudinal resistivity (ρ_{xx}) data, following the procedure established in ref. 18. The subtracted data were then interpolated onto a regular grid for the FFT. For Fig. 1f, the analysis was done using a magnetic field range of ~0.3 T to 1.9 T. For Fig. 3c, we used the range ~0.07 T to 1 T, for Extended Data Fig. 8, the range ~0.09 T to 0.932 T, for Supplementary Information Fig. 5, the range ~0.07 T to 1 T (same data as in Fig. 3c), and for Supplementary Information Fig. 7, the range ~0.3 T to 2 T. The magnetic field range for each fan was chosen to minimize noise in the FFT, without introducing any spurious frequencies. After taking the Fourier transform, we normalized the raw frequencies by the Luttinger volume $n(h/e)$. The normalized frequency f_ν then corresponded to the fraction of the total Fermi surface enclosed by a cyclotron orbit in momentum space[9]. Consequently, the sum of all frequencies was 1 when the appropriate carrier sign, isospin degeneracies and Fermi-surface topologies are considered.

The code we used to analyse the FFTs is based on the code in ref. 9. To extract the relevant frequencies, we placed each FFT on an interactive grid in which individual trajectories were fitted by a user directly selecting them. We used this method to fill an array of grid coordinates, which we then fitted to a polynomial. A step-by-step analysis is shown in Extended Data Fig. 8. In our FFT analysis, we used the following colour and line conventions: solid curves denote frequencies, which we directly fitted using the method described above (or frequencies that directly correspond to an unchanging fraction such as 1/4), and dashed curves were derived from the solid curves, either through multiplication or the addition or subtraction of a relevant fraction (for annular Fermi surfaces, see, for example, Fig. 3c). Curves (or pairs of curves) are colour-coded based on the corresponding implied Fermi-surface degeneracy, with red corresponding to 4, blue corresponding to 2, and black corresponding to other or unknown. We additionally used magenta in Supplementary Information Fig. 7 to colour-code a more complicated set of frequencies that combine to equal 1. We attempted to characterize all the prominent trajectories in each plot, and the analysis shown represents our best interpretation. However, certain regions of the fans, where the FFTs are too complicated to analyse, are left without fits. We note that an interpretation of FFTs may be ambiguous in regions of parameter space with the potential for a combination of overlapping valence and conduction bands, annular or disjoint Fermi surfaces, and isospin polarization in one or both bands.

Self-consistent mean-field calculation

We present the theory for the misaligned octalayer system here and relegate the theory for the moiré heptalayer system to the Supplementary Information[50–55]. To model the band structure of N_ℓ-layer rhombohedral graphene without a moiré structure, we adopt the conventional tight-binding parameterization, wherein the Hamiltonian in the sublattice basis $\{A_1, B_1, A_2, B_2, \ldots, A_{N_\ell}, B_{N_\ell}\}$ is given by[1–5,56]

$$\mathbb{K}_{N_\ell}(\mathbf{k}) = \begin{pmatrix} \mathbb{K}_1(\mathbf{k}) & \mathbb{U}_{\mathrm{nl}}(\mathbf{k}) & \mathbb{U}_{\mathrm{nnl}} & \ldots & \mathbb{0} \\ \mathbb{U}_{\mathrm{nl}}^\dagger(\mathbf{k}) & \mathbb{K}_1(\mathbf{k}) & \mathbb{U}_{\mathrm{nl}}(\mathbf{k}) & \ldots & \mathbb{0} \\ \mathbb{U}_{\mathrm{nnl}}^\dagger & \mathbb{U}_{\mathrm{nl}}^\dagger(\mathbf{k}) & \mathbb{K}_1(\mathbf{k}) & \ldots & \mathbb{0} \\ \vdots & \vdots & \vdots & \ddots & \mathbb{0} \\ \mathbb{0} & \mathbb{0} & \mathbb{0} & \ldots & \mathbb{K}_1(\mathbf{k}) \end{pmatrix} + \delta_{\mathrm{dimer}} \begin{pmatrix} \sigma_- & \mathbb{0} & \ldots & \mathbb{0} & \mathbb{0} \\ \mathbb{0} & \mathbb{1} & \ldots & \mathbb{0} & \mathbb{0} \\ \vdots & \vdots & \ddots & \vdots & \vdots \\ \mathbb{0} & \mathbb{0} & \ldots & \mathbb{1} & \mathbb{0} \\ \mathbb{0} & \mathbb{0} & \ldots & \mathbb{0} & \sigma_+ \end{pmatrix}, \tag{1}$$

where $\sigma_\pm$ are the Pauli lowering (−) and raising (+) operators. The 2×2 matrices $\mathbb{K}_1$, $\mathbb{U}_{\mathrm{nl}}$ and $\mathbb{U}_{\mathrm{nnl}}$ are the single-layer graphene Hamiltonian, nearest-layer hopping matrix and next-nearest-layer hopping matrix respectively:

$$\begin{aligned} \mathbb{K}_1(\mathbf{k}) &= \begin{pmatrix} 0 & -\gamma_0 f(\mathbf{k}) \\ -\gamma_0 f^\dagger(\mathbf{k}) & 0 \end{pmatrix}, \\ \mathbb{U}_{\mathrm{nl}}(\mathbf{k}) &= \begin{pmatrix} -\gamma_4 f(\mathbf{k}) & -\gamma_3 f^\dagger(\mathbf{k}) \\ \gamma_1 & -\gamma_4 f(\mathbf{k}) \end{pmatrix}, \\ \mathbb{U}_{\mathrm{nnl}} &= \begin{pmatrix} 0 & \gamma_2/2 \\ 0 & 0 \end{pmatrix}, \end{aligned} \tag{2}$$

where $f(\mathbf{k}) = \sum_{i\in\{1,2,3\}} e^{i\mathbf{k}\cdot\boldsymbol{\delta}_i}$, $\boldsymbol{\delta}_1 = a/\sqrt{3}(0,1)$, $\boldsymbol{\delta}_2 = a/\sqrt{3}(-\sqrt{3}/2, -1/2)$, $\boldsymbol{\delta}_3 = a/\sqrt{3}(\sqrt{3}/2, -1/2)$, $a = 2.46$ Å is the lattice constant, $\{\gamma_0, \gamma_1, \gamma_2, \gamma_3, \gamma_4\} = \{3.1, 0.38, -0.015, -0.29, -0.141\}$ eV are the hopping constants, and $\delta_{\mathrm{dimer}} = 10.5$ meV is the dimerization energy on the eclipsed sites $B_1, A_2, B_2, \ldots, A_{N_\ell-1}, B_{N_\ell-1}, A_{N_\ell}$ (only A_1 and B_{N_ℓ} are not eclipsed)[18]. The layer-dependent on-site potential energy due to a vertical displacement field is added to the Hamiltonian using the following potential:

$$\mathbb{\Delta} = \frac{\Delta}{2} \begin{pmatrix} +(N_\ell - 1)\mathbb{1} & \mathbb{0} & \ldots & \mathbb{0} \\ \mathbb{0} & +(N_\ell - 3)\mathbb{1} & \ldots & \mathbb{0} \\ \vdots & \vdots & \ddots & \vdots \\ \mathbb{0} & \mathbb{0} & \ldots & -(N_\ell - 1)\mathbb{1} \end{pmatrix}, \tag{3}$$

where Δ is the energy difference between two consecutive layers. The energy difference across the entire N_ℓ-layer stack is $\Delta(N_\ell - 1)$.

To account for band renormalization due to electron–electron interactions, we implemented the self-consistent mean-field theory within the Hartree–Fock approximation. The mean-field Hamiltonian in second-quantized notation is

$$\begin{aligned} \hat{\mathcal{H}}_{\mathrm{HF}} = \sum_{\mathbf{k},\alpha,\ell,\alpha',\ell'} \hat{c}^\dagger_{\alpha,\ell,\mathbf{k}} \big[&\mathbb{K}^{\alpha,\ell,\alpha',\ell'}(\mathbf{k}) \\ &+ \mathbb{H}^{\alpha,\ell,\alpha',\ell'} + \mathbb{F}^{\alpha,\ell,\alpha',\ell'}(\mathbf{k}) \big] \hat{c}_{\alpha',\ell',\mathbf{k}}. \end{aligned} \tag{4}$$

Here $\hat{c}^\dagger_{\alpha,\ell,\mathbf{k}}$ is the creation operator for a plane-wave state with α quantum numbers, where α is a multi-index label that includes the valley ξ, spin s and sublattice σ on layer ℓ and with momentum $\mathbf{k}$. $\mathbb{K}^{\alpha,\ell,\alpha',\ell'}(\mathbf{k})$ is the same as $\mathbb{K}_{N_\ell}(\mathbf{k})$ with internal indices explicitly specified. The Hartree and Fock matrices are given by

$$\begin{aligned} \mathbb{H}^{\alpha,\ell,\alpha',\ell'} &= +\frac{\delta_{\alpha,\alpha'}\delta_{\ell,\ell'}}{V_{\mathrm{sys}}} \sum_{\mathbf{p},\beta,\ell''} \mathcal{V}_{\ell,\ell''}(\mathbf{0}) \mathbb{D}^{\beta,\ell'',\beta,\ell''}(\mathbf{p}), \\ \mathbb{F}^{\alpha,\ell,\alpha',\ell'}(\mathbf{k}) &= -\frac{1}{V_{\mathrm{sys}}} \sum_{\mathbf{p}} \mathcal{V}_{\ell,\ell'}(\mathbf{p}-\mathbf{k}) \mathbb{D}^{\alpha,\ell,\alpha',\ell'}(\mathbf{p}), \end{aligned} \tag{5}$$

where V_{sys} is the volume of the system. We have defined a density matrix $\mathbb{D}^{\alpha,\ell,\alpha',\ell'}(\mathbf{k}) = \langle \hat{c}^{\dagger}_{\alpha',\ell',\mathbf{k}} \hat{c}_{\alpha,\ell,\mathbf{k}} \rangle$. Note the order of the indices in our definition of the density matrix. Explicitly, the matrix elements can be calculated from the coefficients of the one-particle eigenstates $\mathbb{D}^{\alpha,\ell,\alpha',\ell'}(\mathbf{k}) = \sum_{n\in\text{occupied}} \phi^{(n)}_{\alpha,\ell,\mathbf{k}} \phi^{(n)*}_{\alpha',\ell',\mathbf{k}}$, where the eigenstates written in terms of plane-wave basis functions $|\psi_{\alpha,\ell,\mathbf{k}}\rangle$ are given by $|\psi^{(n)}_{\mathbf{k}}\rangle = \sum_{\alpha,\ell} \phi^{(n)}_{\alpha,\ell,\mathbf{k}} |\psi_{\alpha,\ell,\mathbf{k}}\rangle$ and n labels the band index. Normalization requires $\sum_{\alpha,\ell} |\phi^{(n)}_{\alpha,\ell,\mathbf{k}}|^2 = 1$. To avoid over-counting the effects of Coulomb interactions already included in ab initio calculations, we subtracted from the density matrices in equation (5) a uniform background density: $\mathbb{D} \mapsto \mathbb{D} - \mathbb{D}_{\text{ref}}$, where $\mathbb{D}^{\alpha,\ell,\alpha',\ell'}_{\text{ref}}(\mathbf{p}) = \frac{1}{2}\delta_{\ell,\ell'}\delta_{\alpha,\alpha'}$ (refs. 57,58).

In a multilayer system, especially one with many layers, charges can reorganize across the layers to oppose the externally applied displacement field. To model this effect, we used a layer-dependent Coulomb potential (for example, see ref. 59 for a derivation)

$$\mathcal{V}_{\ell,\ell'}(\mathbf{q}) = \frac{e^2 \operatorname{csch}(|\mathbf{q}|d_g)}{2\epsilon_0\epsilon_r|\mathbf{q}|}\left[\cosh\left(|\mathbf{q}|\{d_g - |z_\ell - z_{\ell'}|\}\right) - \cosh\left(|\mathbf{q}|\{d_g - |z_\ell + z_{\ell'}|\}\right)\right], \tag{6}$$

where e is the electric charge, $\epsilon_0\epsilon_r$ is the dielectric constant, d_g is the distance between the top and bottom gates, and z_ℓ is the vertical height of the ℓ layer measured from the bottom gate at $z = 0$. The $\mathbf{k} = 0$ component of this potential,

$$\mathcal{V}_{\ell,\ell'}(\mathbf{0}) = \lim_{\mathbf{q}\to\mathbf{0}} \mathcal{V}_{\ell,\ell'}(\mathbf{q}) = \frac{e^2}{\epsilon_0\epsilon_r}\left[\min(z_\ell, z_{\ell'}) - \frac{z_\ell z_{\ell'}}{d_g}\right], \tag{7}$$

reproduces the screening of uniform charges in a classical capacitor model[60]. In this work, we use $d_g = 40$ nm and assume that the graphene stack is located symmetrically between the two gates. The dielectric constant was chosen to be $\epsilon_r = 16$ to reproduce the onset of the insulating behaviour at charge neutrality seen in the experiment. As our calculation does not directly compute internal screening due to both active (involved in the Hartree–Fock approximation) and remote bands, this higher value of ϵ_r compared with the known values of the dielectric constant of hBN allows us to qualitatively account for screening, not only from the dielectric environment but also between the electrons themselves[61].

In the numerical simulation, we determined equation (4) iteratively. We imposed an ultraviolet cutoff by choosing a regular hexagonal region in reciprocal space centred at each valley $K_\xi = \xi(4\pi/3a, 0)$ with sides equal to $0.1 \times |K_\xi| = 0.17$ Å^{-1}. Inside each such region, $3N_{\mathbf{k}}(N_{\mathbf{k}} + 1) + 1$ points were sampled in the calculation. We chose $N_{\mathbf{k}} = 70$, which means that our grid contains 14,911 points per valley and spin. In this work, we did not search for symmetry-broken states; therefore, our ansatz is always the symmetric state where all isospins are filled equally. To facilitate faster convergence, at each step, we used a weighted average of the two most recent density matrices. To calculate the layer-resolved DOS and the total DOS, we used the following approximations:

$$\text{DOS}_\ell(\varepsilon) = \frac{1}{\pi}\sum_{n,\mathbf{k}}\left[\sum_\alpha |\phi^{(n)}_{\alpha,\ell,\mathbf{k}}|^2\right]\frac{\eta}{\eta^2 + (\varepsilon - \varepsilon_{n,\mathbf{k}})^2}, \tag{8a}$$

$$\text{DOS}(\varepsilon) = \sum_\ell \text{DOS}_\ell(\varepsilon), \tag{8b}$$

where η is a broadening factor chosen to be 1–2 meV. These definitions have units of inverse energy; there is no factor of $1/V_{sys}$ as we have integrated over the lateral directions. The small broadening factor is necessary to produce a smooth evolution of the DOS in the phase diagram, as our simulation mesh is necessarily granular (although it is very large, as aforementioned).

Theoretical determination of the displacement field

The experimental phase diagrams are plotted as a function of the displacement field D, which is related to the top- and bottom-gate charge densities, σ_t and σ_b. These were extracted experimentally using the gate capacitances. The displacement field is defined as:

$$D = \frac{\sigma_b - \sigma_t}{2\epsilon_0}. \tag{9}$$

In our theoretical calculations, D is not a direct input, but is instead represented only by its proxy Δ. To translate between the two quantities so that the theoretical calculations can be compared with the experimental data, we used the Hartree approximation wherein we assumed that D is determined only by the average uniform charge density on each layer. That is, the charge variation on the unit-cell scale does not matter[62,63]. Let us denote $D_{\ell,\ell'}$ the displacement field between layers ℓ and ℓ'. By Gauss's law, we, therefore, have

$$\frac{\sigma_\ell}{\epsilon_0} = D_{\ell-1,\ell} - D_{\ell,\ell+1}, \tag{10}$$

where σ_ℓ is the charge density of layer ℓ. Here $\ell \in \{1, \ldots, N_\ell\}$ denotes graphene layers, and $\ell = 0$ is the top gate and $\ell = N_\ell + 1$ is the bottom gate. Charge neutrality enforces $\sum_{\ell=0}^{N_\ell+1}\sigma_\ell = 0$. Substituting equation (10) into equation (9), we found

$$D = \frac{D_t + D_b}{2}, \tag{11}$$

where $D_t = D_{0,1}$ and $D_b = D_{N_\ell,N_\ell+1}$. We can relate these two fields closest to the gates to any other two fields between the graphene layers. For instance, we can rewrite equation (11) as

$$D = \frac{\sigma_1 - \sigma_{N_\ell}}{2\epsilon_0} + \frac{D_{N_\ell-1,N_\ell} + D_{1,2}}{2}; \tag{12}$$

more generally, for any $n, n' \in \{1, \ldots, N_\ell\}$, we have

$$D = \frac{\sum_{\ell=1}^{n}\sigma_\ell - \sum_{\ell=n'}^{N_\ell}\sigma_\ell}{2\epsilon_0} + \frac{D_{n'-1,n'} + D_{n,n+1}}{2}. \tag{13}$$

The layer charge densities can be calculated by tracing over the converged density matrices. The interlayer displacement fields are calculable from the on-site energies $\varepsilon_\ell = \mathbb{H}^{\alpha,\ell,\alpha,\ell} + \Delta^{\alpha,\ell,\alpha,\ell}$:

$$D_{\ell,\ell+1} = \frac{\epsilon_r}{ed}(\varepsilon_\ell - \varepsilon_{\ell+1}), \tag{14}$$

where $d = 3.35$ Å is the distance between graphene layers. Together, equations (13) and (14) allow us to calculate D for every Δ using the self-consistent mean-field solution at said Δ. We emphasize that, in our approach, once the hopping parameters and dielectric constant, which controls the strength of Coulomb interactions at zero and finite $\mathbf{q}$, are specified (and these are constrained by experimental considerations), D and Δ are unambiguously related to each other by self-consistency.

Data availability

Raw data for Figs. 1–4 and Extended Data Figs. 1–10 are available via Zenodo (https://doi.org/10.5281/zenodo.19675446)[64]. Source data are provided with this paper. All other data that support the findings of this study are available from the corresponding authors upon request.

References

48. Li, H. et al. Electrode-free anodic oxidation nanolithography of low-dimensional materials. *Nano Lett.* **18**, 8011–8015 (2018).

49. Kapitulnik, A., Kivelson, S. A. & Spivak, B. Colloquium: anomalous metals: failed superconductors. *Rev. Mod. Phys.* **91**, 011002 (2019).
50. Kern, G., Kresse, G. & Hafner, J. Ab initio calculation of the lattice dynamics and phase diagram of boron nitride. *Phys. Rev. B* **59**, 8551–8559 (1999).
51. Castro Neto, A. H., Guinea, F., Peres, N. M. R., Novoselov, K. S. & Geim, A. K. The electronic properties of graphene. *Rev. Mod. Phys.* **81**, 109–162 (2009).
52. Sławińska, J., Zasada, I. & Klusek, Z. Energy gap tuning in graphene on hexagonal boron nitride bilayer system. *Phys. Rev. B* **81**, 155433 (2010).
53. Kindermann, M., Uchoa, B. & Miller, D. L. Zero-energy modes and gate-tunable gap in graphene on hexagonal boron nitride. *Phys. Rev. B* **86**, 115415 (2012).
54. Moon, P. & Koshino, M. Electronic properties of graphene/hexagonal-boron-nitride moiré superlattice. *Phys. Rev. B* **90**, 155406 (2014).
55. Jung, J., Raoux, A., Qiao, Z. & MacDonald, A. H. Ab initio theory of moiré superlattice bands in layered two-dimensional materials. *Phys. Rev. B* **89**, 205414 (2014).
56. McClure, J. Electron energy band structure and electronic properties of rhombohedral graphite. *Carbon* **7**, 425–432 (1969).
57. Xie, M. & MacDonald, A. H. Nature of the correlated insulator states in twisted bilayer graphene. *Phys. Rev. Lett.* **124**, 097601 (2020).
58. Bernevig, B. A., Song, Z.-D., Regnault, N. & Lian, B. Twisted bilayer graphene. III. interacting Hamiltonian and exact symmetries. *Phys. Rev. B* **103**, 205413 (2021).
59. Phong, V. T. & Lewandowski, C. Coulomb Interaction-stabilized isolated narrow bands with Chern numbers $\mathcal{C} > 1$ in twisted rhombohedral trilayer-bilayer graphene. Preprint at http://arXiv.org/abs/2505.07981 (2025).
60. Kolář, K., Zhang, Y., Nadj-Perge, S., von Oppen, F. & Lewandowski, C. Electrostatic fate of *n*-layer moiré graphene. *Phys. Rev. B* **108**, 195148 (2023).
61. Parra-Martínez, G. et al. Band renormalization, quarter metals, and chiral superconductivity in rhombohedral tetralayer graphene. *Phys. Rev. Lett.* **135**, 136503 (2025).
62. McCann, E. Asymmetry gap in the electronic band structure of bilayer graphene. *Phys. Rev. B* **74**, 161403 (2006).
63. Gava, P., Lazzeri, M., Saitta, A. M. & Mauri, F. Ab initio study of gap opening and screening effects in gated bilayer graphene. *Phys. Rev. B* **79**, 165431 (2009).
64. Kumar, M. et al. Superconductivity from dual-surface carriers in rhombohedral graphene: Raw data for Main Text and Extended Data [Data set]. *Zenodo* https://doi.org/10.5281/zenodo.19675446 (2026).

Acknowledgements

We thank UBC research associate S. Folk for helpful contributions and R. Waleffe for useful discussions about the FFT analysis code. The research on superconductivity was supported by the Army Research Office (Award No. W911NF-25-1-0012). The work on topology was supported as part of Programmable Quantum Materials, an Energy Frontier Research Center funded by the US Department of Energy, Office of Science, Basic Energy Sciences (Award No. DE-SC0019443). Device fabrication was supported by the US National Science Foundation (NSF) (CAREER Award No. DMR-2041972) and the University of Washington Molecular Engineering Materials Center, an NSF Materials Research Science and Engineering Center (Award No. DMR-2308979). Experiments at the University of British Columbia were undertaken with support from the Natural Sciences and Engineering Research Council of Canada; the Canada Foundation for Innovation; the Canadian Institute for Advanced Research; the Max Planck-UBC-UTokyo Centre for Quantum Materials and the Canada First Research Excellence Fund, Quantum Materials and Future Technologies Program; and the European Research Council under the European Union's Horizon 2020 research and innovation programme (Grant Agreement No. 951541). A.O. and M.Y. acknowledge support from the State of Washington-funded Clean Energy Institute. Numerical calculations were done using the High Performance Compute Cluster of the Research Computing Center at Florida State University. V.T.P. and C.L. are supported by start-up funds from Florida State University and the National High Magnetic Field Laboratory. The National High Magnetic Field Laboratory is supported by the NSF (Award No. NSF/DMR-2128556) and the State of Florida. K.W. and T.T. acknowledge support from the JSPS (KAKENHI Grant Nos. 21H05233 and 23H02052) and the World Premier International Research Center Initiative, MEXT, Japan. This work made use of shared fabrication facilities at UW provided by NSF MRSEC (Award No. 2308979).

Author contributions

M.K. fabricated the samples with assistance from A.O. M.K., D.W. and A.O. led the measurements at UBC remotely, with R.T. assisting on-site. V.T.P. performed the theoretical calculations supervised by C.L. K.W. and T.T. provided the hBN crystals. J.F. and M.Y. supervised the project.

Competing interests

The authors declare no competing interests.

Additional information

Extended data is available for this paper at https://doi.org/10.1038/s41567-026-03277-5.

Supplementary information The online version contains supplementary material available at https://doi.org/10.1038/s41567-026-03277-5.

Correspondence and requests for materials should be addressed to Joshua Folk or Matthew Yankowitz.

Peer review information *Nature Physics* thanks the anonymous reviewers for their contribution to the peer review of this work.

https://doi.org/10.1038/s41567-026-03277-5

Extended Data Table 1 | Summary of key parameters relevant to superconductivity

Pocket	T_c (mK)	B_c (mT)	ξ (nm)
$SC1_7$	89	1.5	470
$SC2_7$	51	2.0	410
$SC1_8$	40	0.65	710
$SC2_8$	67	1.0	570
$SC3_8$	170	0.8	640
$SC4_8$	20	0.15	1,480
$SC5_8$	78	0.32	1,010

Values were extracted following the procedures described in Methods.

https://doi.org/10.1038/s41567-026-03277-5

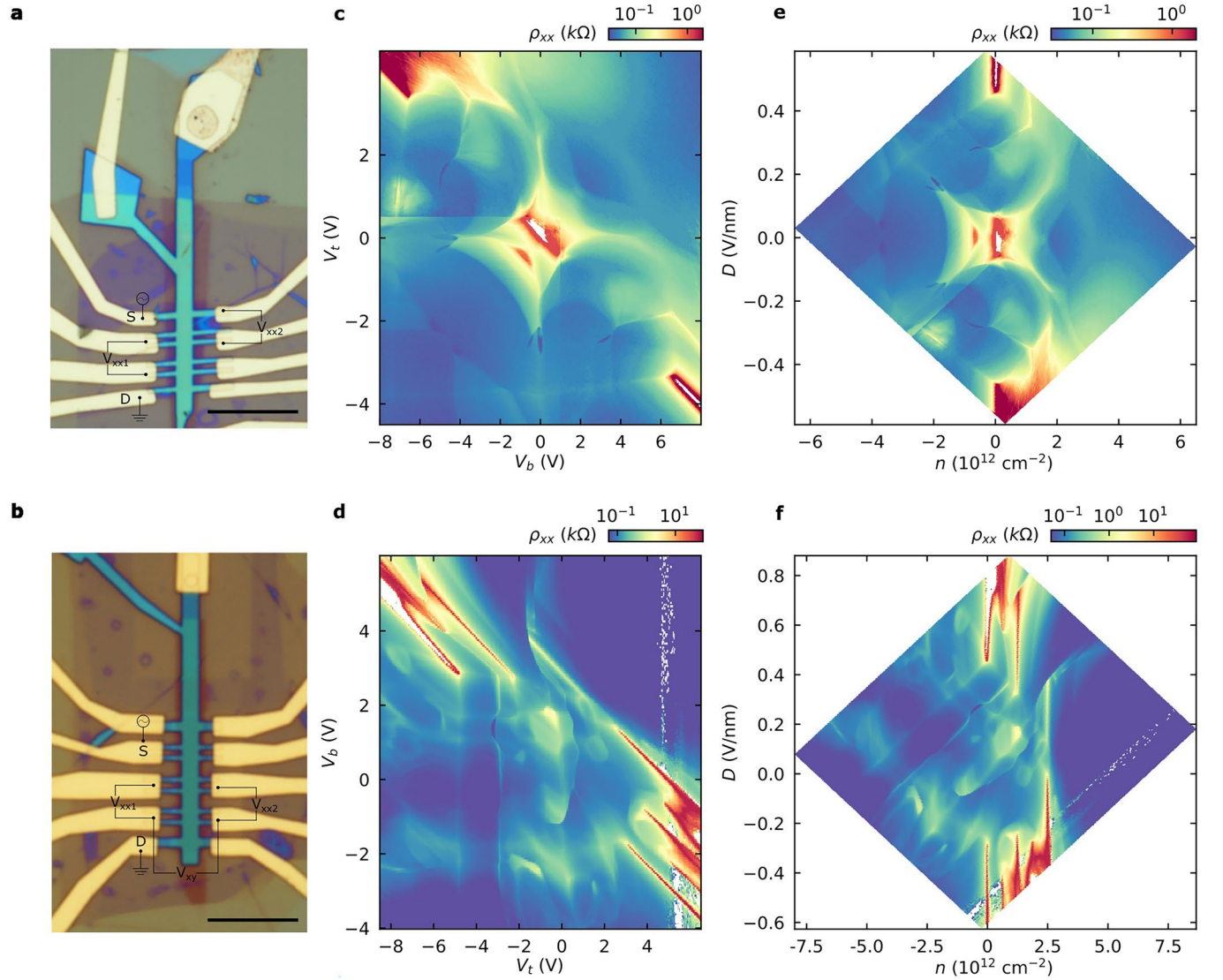

Extended Data Fig. 1 | Optical micrographs and full gate maps of both devices. a, Optical micrograph of the misaligned R8G device. **b**, Same as (**a**) for the moiré R7G device. For both, the scale bar is 10 μm. **c**, Map of ρ_{xx} for the R8G device measured over a wide range of V_b and V_t. The map is acquired in pieces and stitched together, with different silicon gate voltages in order to optimally reduce the contact resistance in each quadrant. **d**, Same as (**c**) for the R7G device. **e**, The map from (**c**) converted to $n - D$ axes (see Methods for conversion). **f**, Same as (**e**) for the R7G device.

https://doi.org/10.1038/s41567-026-03277-5

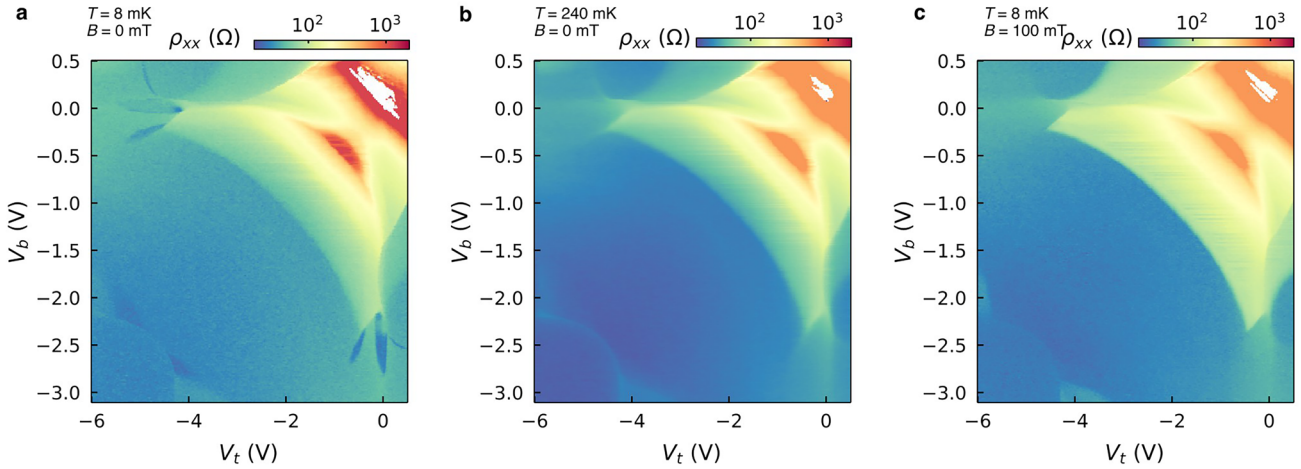

Extended Data Fig. 2 | Transport with varying temperature and magnetic field in the R8G device. a, Map of ρ_{xx} versus V_b and V_t at base temperature and $B = 0$. The highly resistive feature in the top right is the correlated insulator at the CNP surrounding D = 0. Superconducting pockets $SC1_8$ to $SC4_8$, and their corresponding $D < 0$ counterparts, are visible within this region of gate voltage. **b**, The same map as (a) at $T = 240$ mK, above T_c of all the pockets. **c**, The same map as (a) at $B = 100$ mT, above B_c of all the pockets.

https://doi.org/10.1038/s41567-026-03277-5

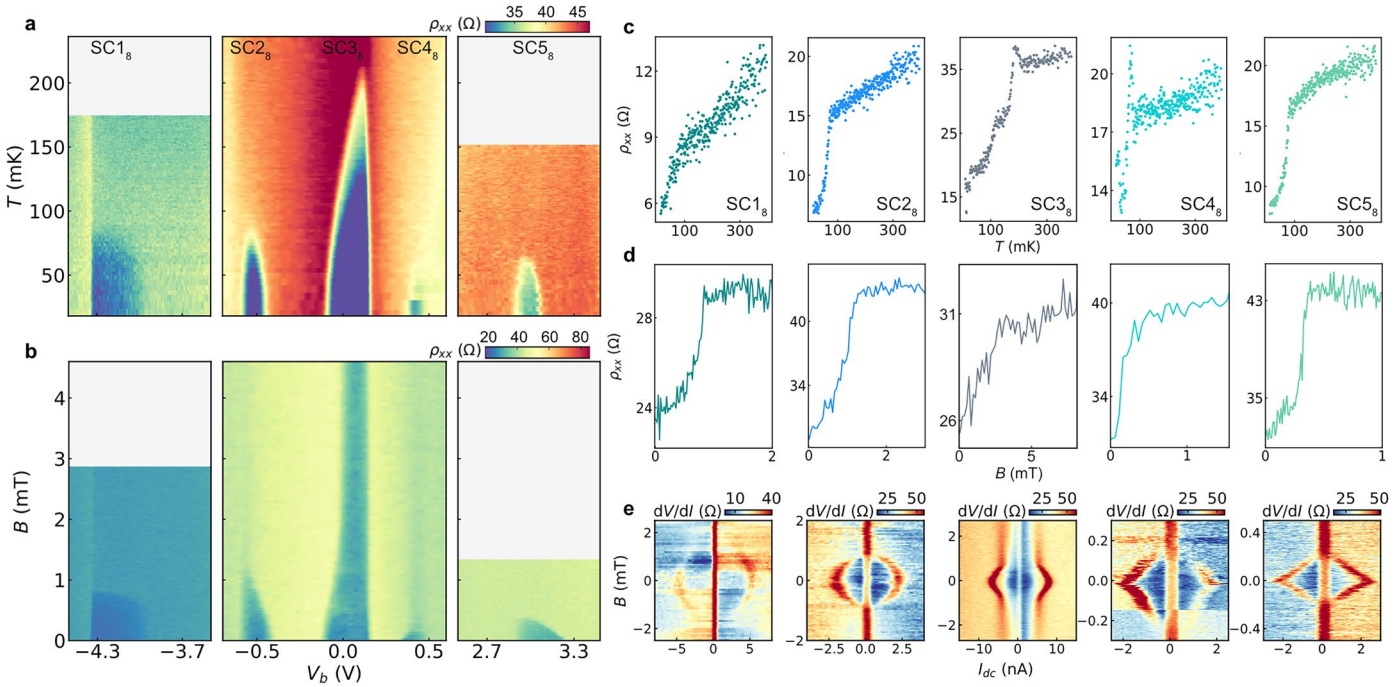

Extended Data Fig. 3 | Additional characterization of SC1$_8$ to SC5$_8$ superconducting pockets in the R8G device. a, Maps of ρ_{xx} versus V_b and T around each pocket, acquired with fixed $V_t = -2.75$ V for SC1$_8$ and $V_t = -2.50$ V for SC2$_8$ - SC5$_8$. **b**, The same maps versus B. **c**, Measurement of ρ_{xx} versus T at optimal doping of each pocket. The measurements are acquired with a small $I_{dc} < 1$ nA to mitigate the effects of a zero-bias anomaly. **d**, The same measurements versus B, with $I_{dc} = 0$. **e**, Maps of dV/dI versus I_{dc} and B for each pocket. In addition to sharp resistive features forming diamond-like structures arising due to superconductivity, there is also an unexpected anomaly at $I_{dc} = 0$.

https://doi.org/10.1038/s41567-026-03277-5

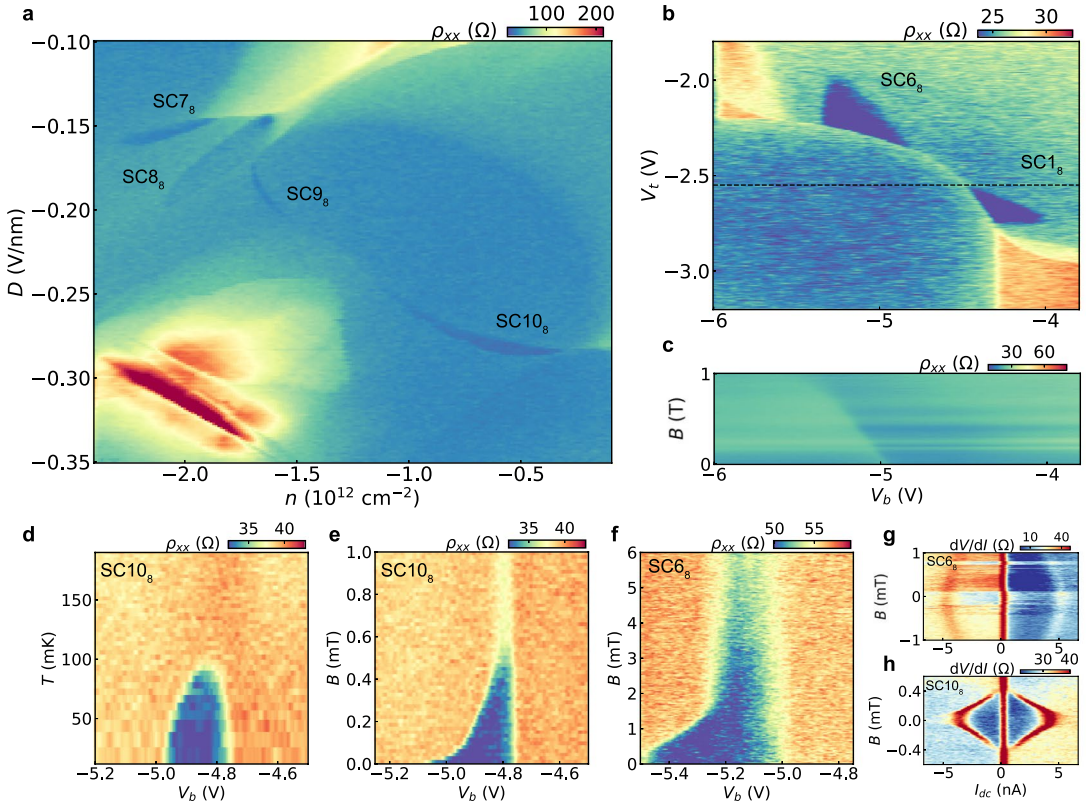

Extended Data Fig. 4 | Additional characterization of superconducting pockets at $D < 0$ in the R8G device. a, Map of ρ_{xx} versus n and D corresponding to $D < 0$. The map contains four superconducting pockets, $SC7_8$ to $SC10_8$, which correspond to $SC2_8$ to $SC5_8$ for $D > 0$. The feature in the bottom left corner exhibits unusual nonlinear behavior and does not appear for $D > 0$; at present, we do not know its origin. **b**, Map of ρ_{xx} versus V_b and V_t showing $SC1_8$ and SC68. **c**, Landau fan diagram taken by sweeping V_b with fixed $V_t = -2.55$ V, corresponding to the black dashed line in (**b**). The sharp resistance step associated with the edge of $SC1_8$ slopes to the left with B, suggestive of a spin-polarized half-metal to the right and an isospin unpolarized phase to the left. **d**, Measurement of ρ_{xx} versus V_b and T at fixed $V_t = 1.6$ V and $B = 0$ for $SC10_8$. **e**, Similar measurement versus B at base temperature. **f**, Similar measurement as (**d**) for the $SC6_8$ pocket at fixed $V_t = -2.2$ V. **g**, Measurement of dV/dI versus I_{dc} and B for $SC6_8$. **h**, Similar measurement for $SC10_8$. Both exhibit the similar zero bias anomalies as seen for the $D > 0$ pockets.

https://doi.org/10.1038/s41567-026-03277-5

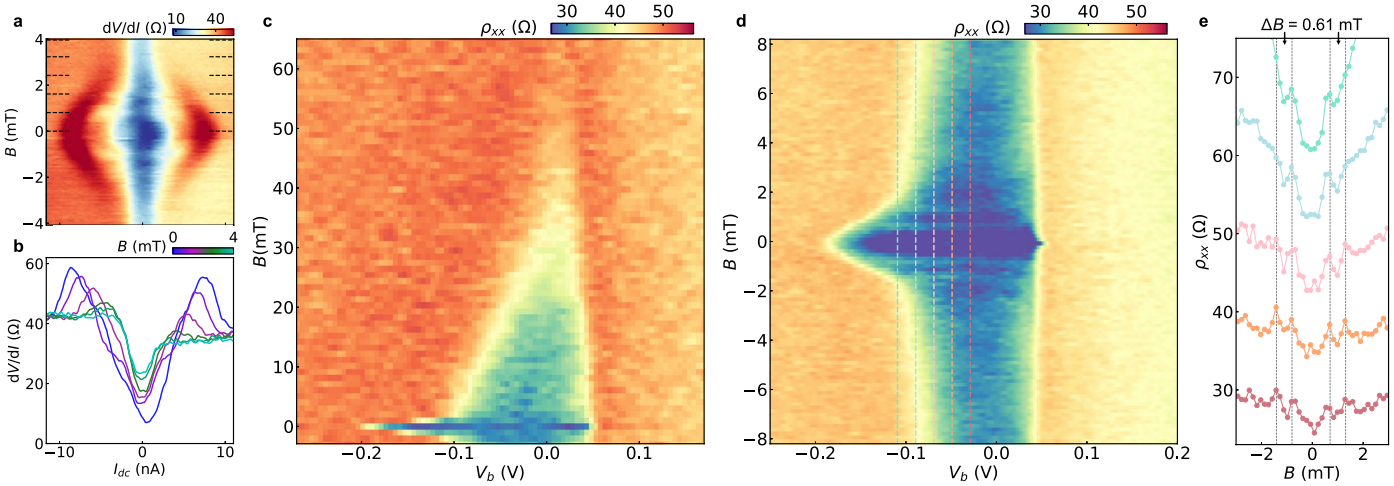

Extended Data Fig. 5 | Additional characterization of $SC3_8$. **a**, Measurement of dV/dI versus I_{dc} and B for $SC3_8$ taken in a subsequent cool-down cycle. **b**, line cuts at B values in (**a**) indicated by the black dashed lines. The absence of a zero-bias peak suggests that its presence in other measurements (Extended Data Figs. 3 and 4) is a contact effect. **c**, Measurement of ρ_{xx} versus V_b and B at fixed $V_t = -2.55$ V for $SC3_8$. There is a sharp suppression of ρ_{xx} very near $B = 0$ corresponding to superconductivity, as well as a weaker suppression persisting up to ≈ 50 mT. The latter likely corresponds to some effect other than superconductivity, although we do not know its origin. **d**, Zoom-in of ρ_{xx} at fixed $V_t = -2.60$ V close to $B = 0$ showing the evolution from a sharp suppression below a few millitesla to a weaker suppression at larger B. **e**, Line cuts corresponding to the dashed lines in (**d**) showing the presence of Fraunhofer oscillations around low B, with a period of 0.61 mT -outlined by the vertical dashed lines.

https://doi.org/10.1038/s41567-026-03277-5

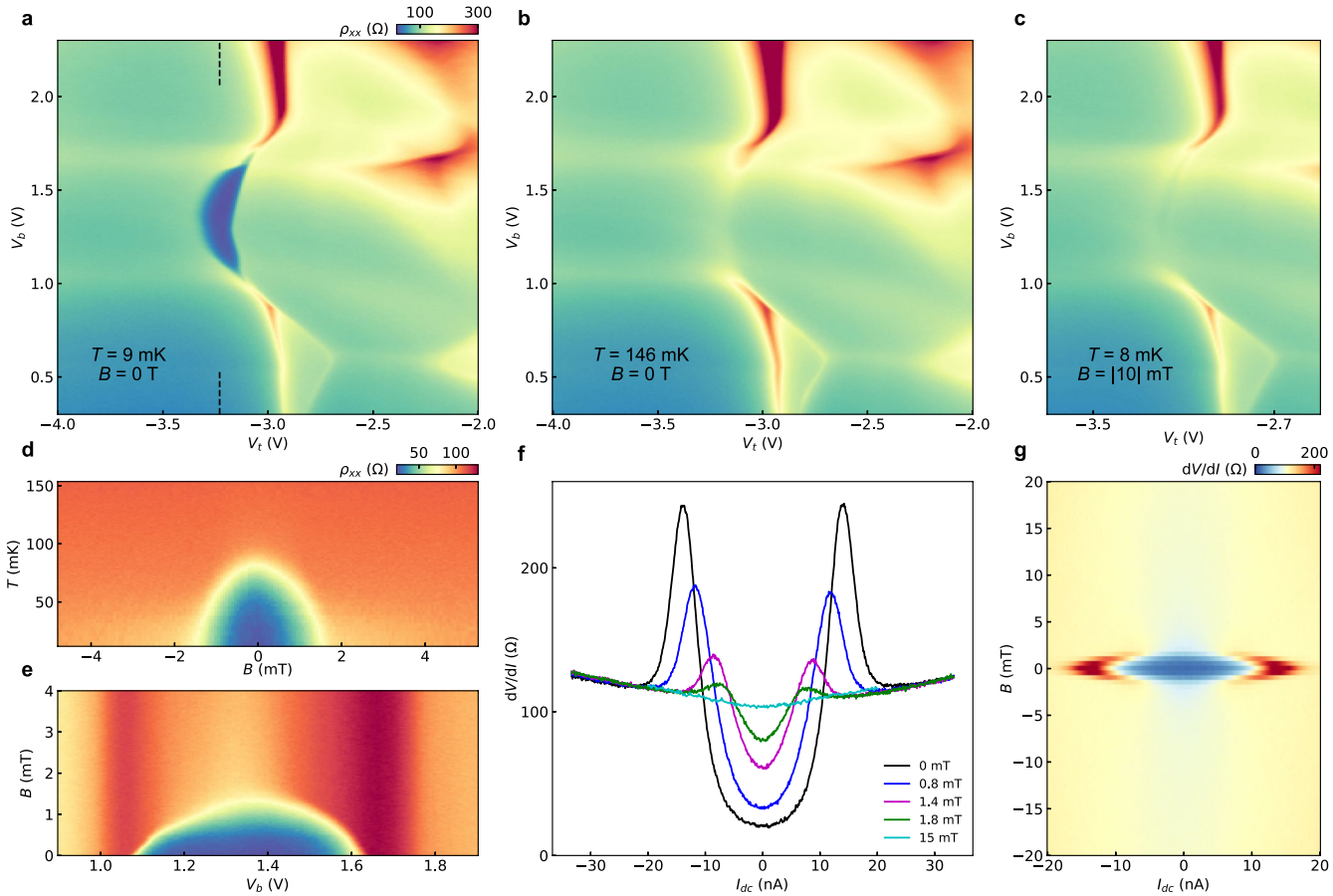

Extended Data Fig. 6 | Additional characterization of the $SC1_7$ pocket from the moiré R7G device. a, Map of ρ_{xx} versus V_b and V_t at base temperature and $B = 0$. **b**, Similar measurement at T = 146 mK, above T_c of $SC1_7$. **c**, Similar measurement, over a narrowed range of V_t, at base temperature and symmetrized at $|B| = 10$ mT, above B_c. **d**, Measurement of ρ_{xx} versus B and T at optimal doping of $SC1_7$ (V_b = 1.40 V and V_t = -3.22 V). **e**, Measurement of ρ_{xx} versus V_b and B at base temperature and fixed V_t = -3.23 V, corresponding to the line trace indicated by black dashed lines in (**a**). In this map, $SC1_7$ is bounded by two resistance bumps associated with nearly constant V_b, that is, the surface associated with the valence band. **f**, Measurements of dV/dI versus I_{dc} at selected values of B taken at optimal doping of $SC1_7$ (V_b = 1.40 V and V_t = -3.22 V). **g**, Map of dV/dI versus I_{dc} and B.

https://doi.org/10.1038/s41567-026-03277-5

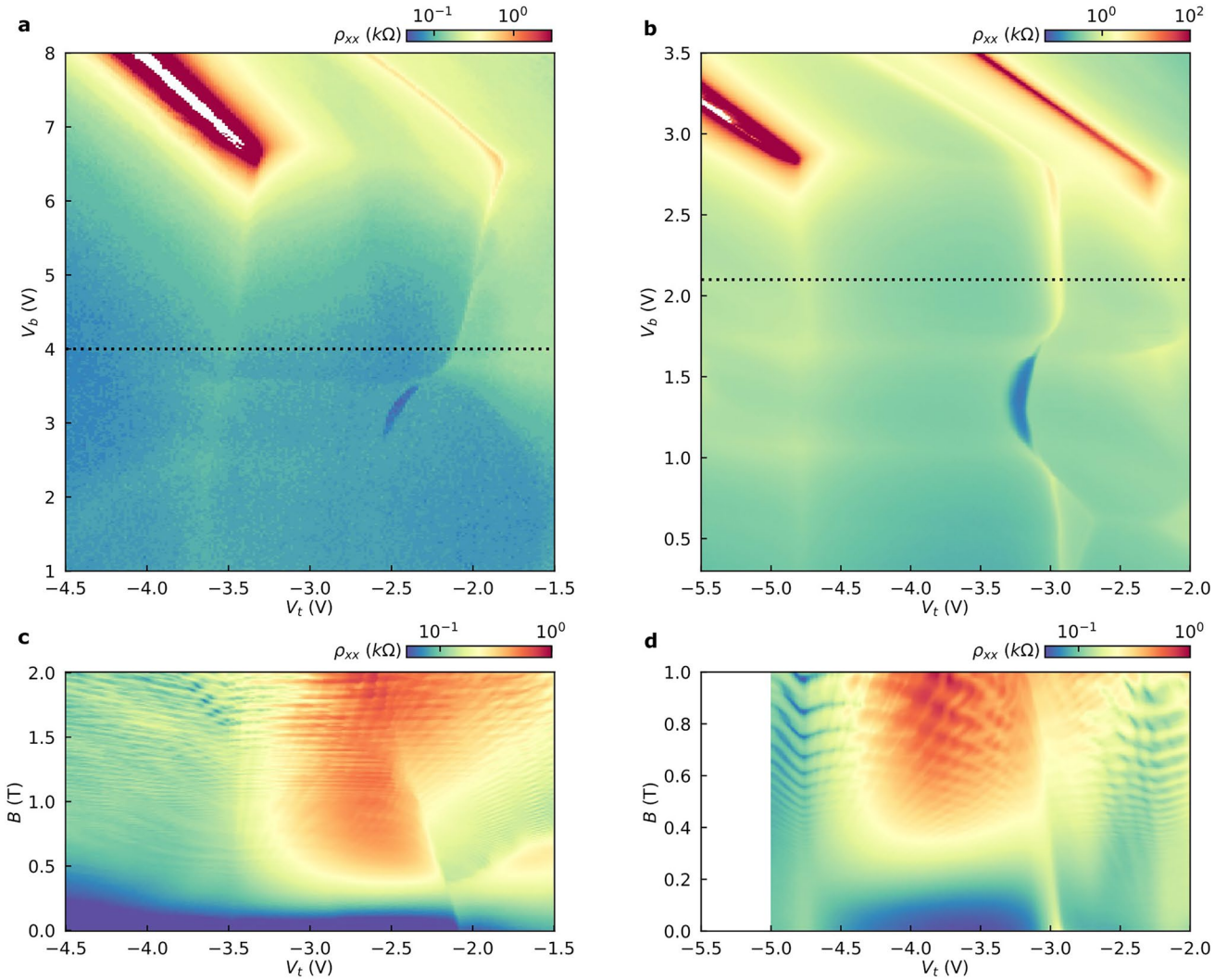

Extended Data Fig. 7 | Comparison of $SC5_8$ from the R8G device and $SC1_7$ from the moiré R7G device. a, Map of ρ_{xx} versus V_b and V_t around $SC5_8$ from the R8G device. **b**, Similar measurement around $SC1_7$ from the R7G device. In both, the diagonal insulating feature in the top left corresponds to the band insulator at the CNP. The resistive feature to its left corresponds is diagonal at large V_b, but becomes nearly vertical at smaller V_b in the band-overlapping regime. In both cases, this feature becomes superconducting when it is intersected by a horizontal resistive bump. the pocket of superconductivity closes when it intersects with a second horizontal resistive bump at smaller V_b. The similarities of these two pockets suggests they share similar origins. **c**, Landau fan taken by sweeping V_t at fixed $V_b = 4.00$ V, along the black dashed line in (**a**). **d**, Landau fan taken by sweeping V_t at fixed $V_b = 2.10$ V, along the black dashed line in (**b**). In both, the sharp resistive bump feature that develops into superconductivity drifts to the left with B, consistent with a spin-polarized half-metal to the right gaining Zeeman energy over an unpolarized phase to the left.

https://doi.org/10.1038/s41567-026-03277-5

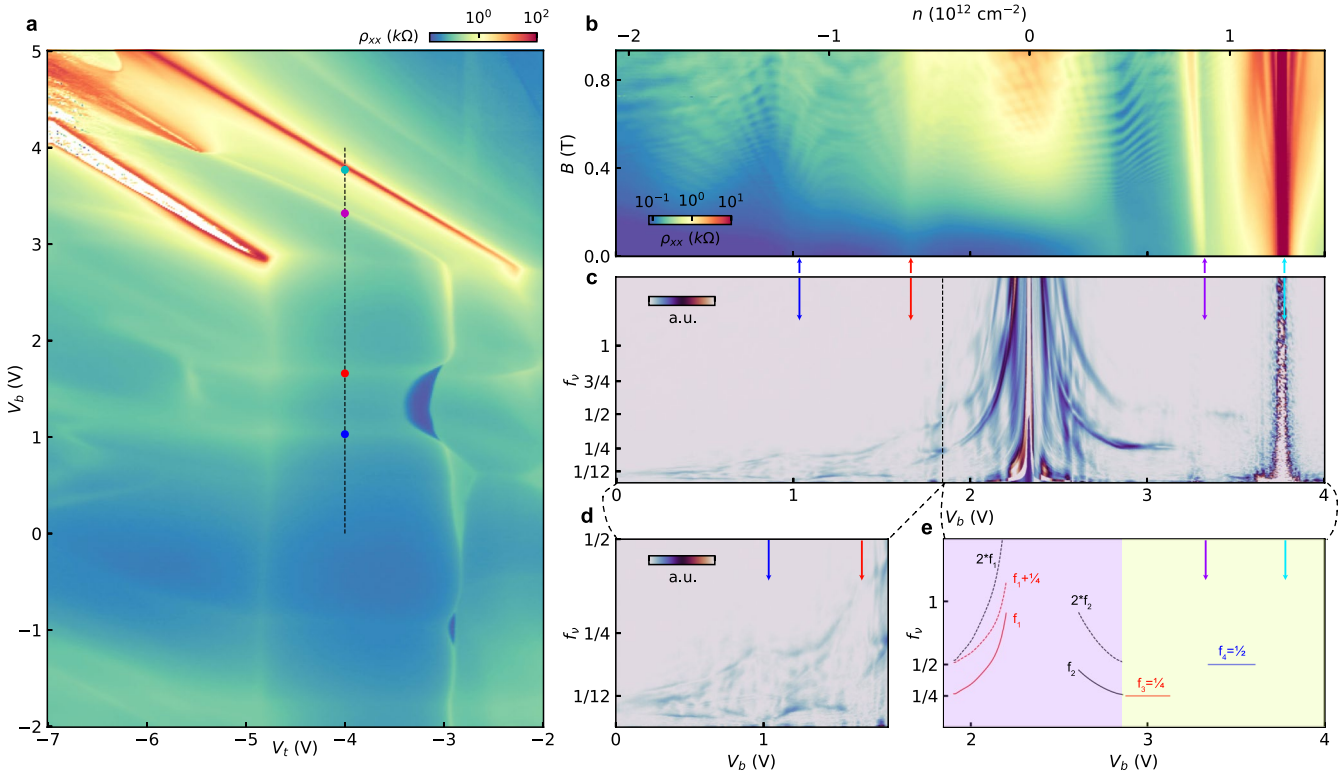

Extended Data Fig. 8 | Additional Fermiology analysis for the moiré R7G device. a, Map of ρ_{xx} versus V_b and V_t taken at base temperature and $B = 0$. **b**, Landau fan taken by sweeping V_b at fixed $V_t = -4$ V, corresponding to the black dashed line in (**a**). Red, blue, purple, and cyan arrows denote the positions of key features, corresponding to the red, blue, purple, and cyan dots from (**a**). c, FFT of the Landau fan. **d**, Zoom-in of the FFT between $V_b = 0$ and 1.84 V. The dominant frequencies in the FFT abruptly change between the red and blue arrows, indicating a Fermi surface reconstruction in the region where $SC1_7$ forms at nearby V_t. **e**, Schematic of the dominant frequencies from the FFT between $V_b = 1.84$ V and 4.00 V. For $V_b > 2.8$ V, corresponding to crossing the jet, the dominant frequency is 0.25 indicating a single, simply-connected Fermi surface from the conduction band. For $V_b > 3.32$ V, upon crossing the sharp resistive bump feature associated with superconductivity and the IQAH state, the dominant frequency shifts to 0.5, indicating a half-metal state. The associated feature drifts to the left in the Landau fan, consistent with a spin-polarized half-metal state.

https://doi.org/10.1038/s41567-026-03277-5

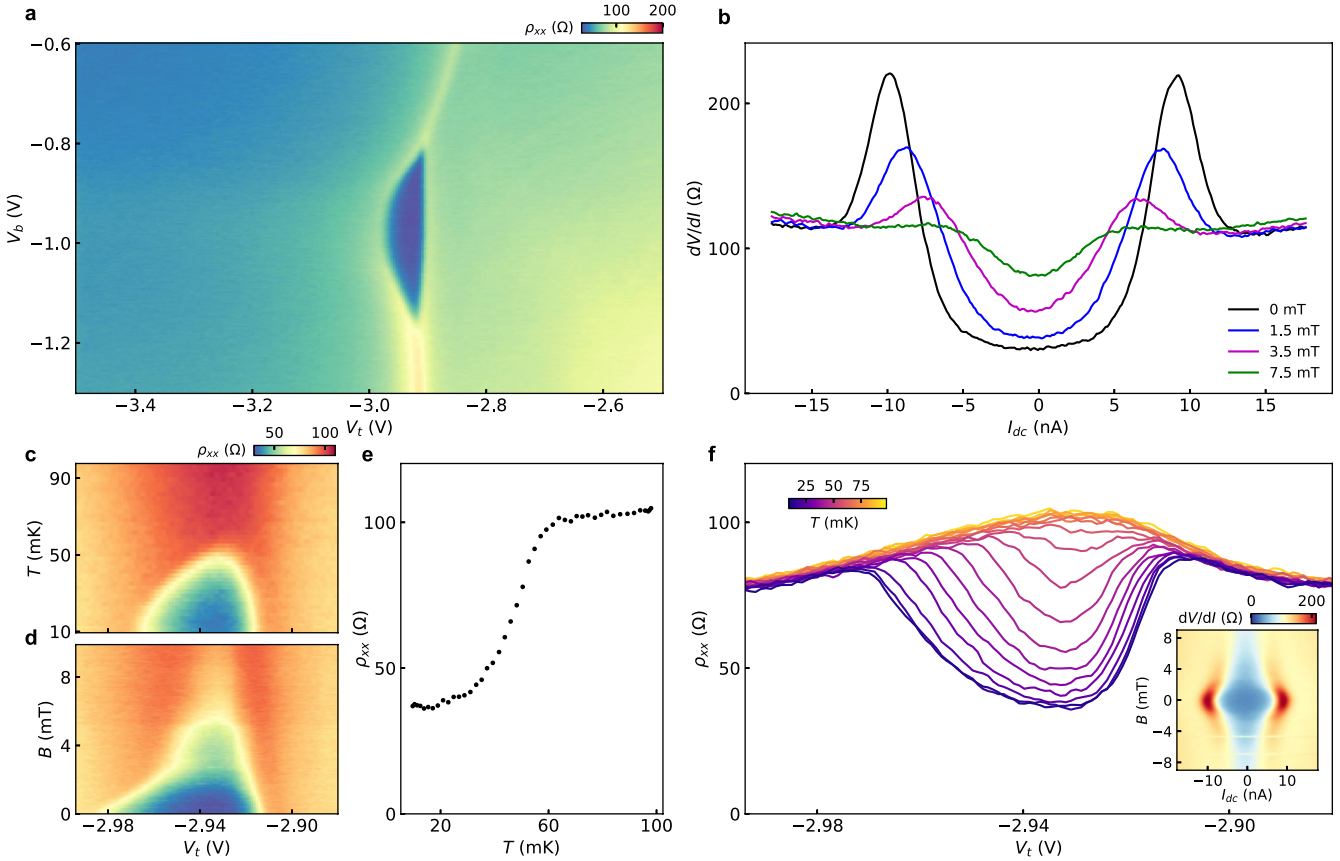

Extended Data Fig. 9 | Additional characterization of the $SC2_7$ pocket from the moiré R7G device. a, Map of ρ_{xx} versus V_b and V_t. **b**, Measurements of dV/dI versus I_{dc} for several selected values of B. **c**, Measurement of ρ_{xx} versus V_t and T at fixed $V_b = -0.95$ V and $B = 0$. **d**, Similar measurement as (**c**) versus B at base temperature. **e**, Measurement of ρ_{xx} versus T (taken at $V_b = -0.95$ V and $V_t = -2.93$ V). **f**, Measurement of ρ_{xx} versus V_t at several selected values of T. (Inset) Map of dV/dI versus I_{dc} and B (taken at $V_b = -0.95$ V and $V_t = -2.93$ V).

https://doi.org/10.1038/s41567-026-03277-5

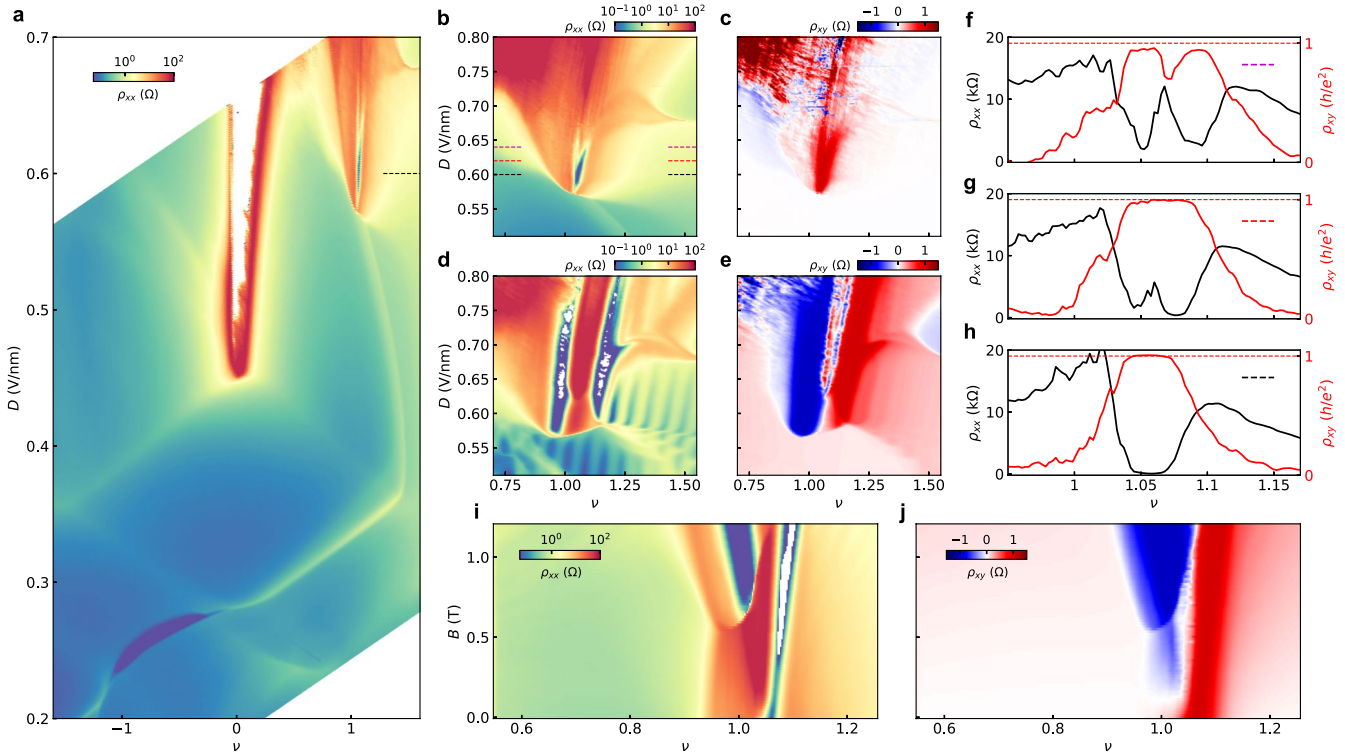

Extended Data Fig. 10 | Additional analysis of the IQAH state in the moiré R7G device. a, Map of ρ_{xx} versus ν and D taken at base temperature and $B = 0$. **b**, Zoom-in of the region around $\nu = 1$ at large D($B = 0$). **c**, Map of ρ_{xy} over the same region as (b) ($B = 0$). **d**, Same as (**b**) symmetrized at $B = 2$ T. **e**, Same as (**c**) antisymmetrized at $B = 2$ T. **f-h**, Measurements of ρ_{xx} and ρ_{xy} versus ν taken at $B = 0$ at the positions of the corresponding color-coded dashed lines in (**b**). At $D = 0.60$ V/nm there is a single contiguous region near $\nu = 1.05$ with $\rho_{xy} \approx h/e^2$ and small ρ_{xx}. At larger D, the state splits into two, with a resistive bump separating them. **i**, Landau fan of ρ_{xx} taken at $D = 0.6$ V/nm, corresponding to the black dashed line in (**a**). **j**, The same measurement as (**i**), but of ρ_{xy}. The fans show the $C = +1$ state arising from $B = 0$, and the abrupt emergence of a $C = -1$ state above $B \approx 0.6$ T. The coexistence of these two states at modest B can also be seen from the maps in (**d**)-(**e**).